iScience

CellPress
OPEN ACCESS

Article

MyoD induces ARTD1 and nucleoplasmic poly-ADP-ribosylation during fibroblast to myoblast transdifferentiation

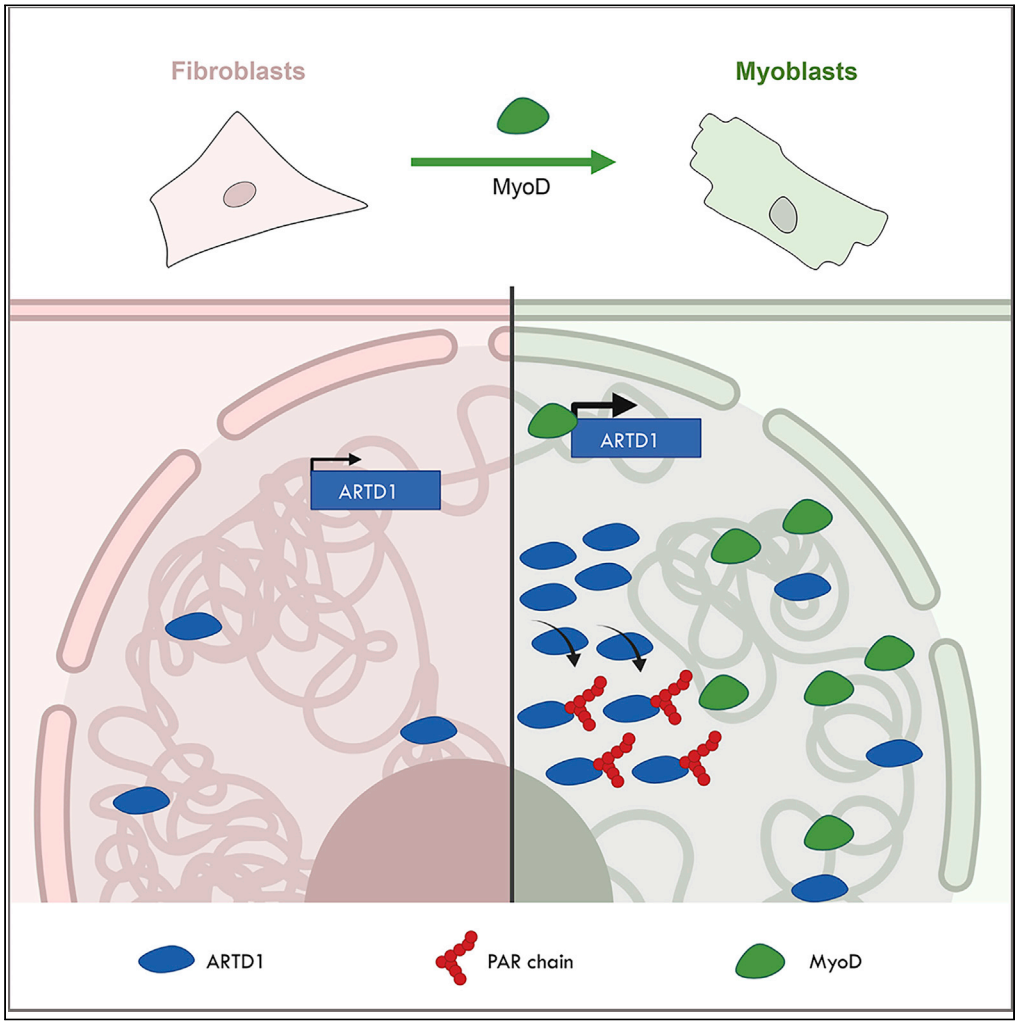

Lavinia Bisceglie, Ann-Katrin Hopp, Kapila Gunasekera, ..., Pier Lorenzo Puri, Miguel Beato, Michael O. Hottiger

michael.hottiger@dmmd.uzh.ch

Highlights

MyoD-dependent transdifferentiation of IMR90 to myoblasts induces ARTD1 expression

Transdifferentiation induces nuclear ARTD1-dependent ADP-ribosylation in myoblasts

This ADP-ribosylation is induced independent of cell cycle and of DNA damage

ARTD1-mediated poly-ADP-ribosylation localizes to the nucleoplasm in myoblasts

Bisceglie et al., iScience 24, 102432
May 21, 2021
https://doi.org/10.1016/j.isci.2021.102432

iScience

CellPress
OPEN ACCESS

Article

MyoD induces ARTD1 and nucleoplasmic poly-ADP-ribosylation during fibroblast to myoblast transdifferentiation

Lavinia Bisceglie,[1,2] Ann-Katrin Hopp,[1] Kapila Gunasekera,[1] Roni H. Wright,[3,4] François Le Dily,[3] Enrique Vidal,[3] Alessandra Dall'Agnese,[5] Luca Caputo,[5] Chiara Nicoletti,[5] Pier Lorenzo Puri,[5] Miguel Beato,[3,6] and Michael O. Hottiger[1,7,*]

SUMMARY

While protein ADP-ribosylation was reported to regulate differentiation and dedifferentiation, it has so far not been studied during transdifferentiation. Here, we found that MyoD-induced transdifferentiation of fibroblasts to myoblasts promotes the expression of the ADP-ribosyltransferase *ARTD1*. Comprehensive analysis of the genome architecture by Hi-C and RNA-seq analysis during transdifferentiation indicated that ARTD1 locally contributed to A/B compartmentalization and coregulated a subset of MyoD target genes that were however not sufficient to alter transdifferentiation. Surprisingly, the expression of ARTD1 was accompanied by the continuous synthesis of nuclear ADP ribosylation that was neither dependent on the cell cycle nor induced by DNA damage. Conversely to the H_2O_2-induced ADP-ribosylation, the MyoD-dependent ADP-ribosylation was not associated to chromatin but rather localized to the nucleoplasm. Together, these data describe a MyoD-induced nucleoplasmic ADP-ribosylation that is observed particularly during transdifferentiation and thus potentially expands the plethora of cellular processes associated with ADP-ribosylation.

INTRODUCTION

Transdifferentiation is the conversion of a fully differentiated cell type into another type without dedifferentiation and reacquisition of progenitor-like features (Mills et al., 2019). Unlike other types of transdifferentiation that rely on the co-operation of multiple transcription or chemical factors (Ieda et al., 2010; Mollinari et al., 2018), MyoD is sufficient to convert fibroblasts and other cell types to myoblasts (Davis et al., 1987; Sartorelli and Puri, 2018; Choi et al., 1990; Weintraub et al., 1989). However, MyoD alone fails to transdifferentiate HeLa (Weintraub et al., 1989), HepG2 (Weintraub et al., 1989), or P19 cells (Skerjanc et al., 1994), suggesting that the chromatin landscape of the initial cell type affects the accessibility of the DNA binding sites of MyoD (i.e. E boxes) and thus its ability to induce the myogenic program (Sartorelli and Puri, 2018). Moreover, trimethylation of histone 3 lysine 27 (H3K27me3) reduced the binding ability of MyoD to chromatin (Caretti et al., 2004; Sartorelli and Puri, 2018) and depletion of polycomb repressor complex 2 (PRC2) increased MyoD-dependent cell-type conversion (Patel et al., 2012) highlighting that histone post-translational modifications (PTMs) plays a crucial role in tuning transdifferentiation. This is supported by the observation that in some epigenetic contexts, the interaction of MyoD with the pioneer factor Pbx overcomes the limitations associated with the accessibility of the E boxes (Berkes et al., 2004; Maves et al., 2007). Moreover, components of the SWItch/Sucrose Non-Fermentable (SWI/SNF) complex, for example, Brg1 and ATPase Brahma, are essential for successful fibroblasts to myoblasts conversion (de la Serna et al., 2001), and human embryonic stem cells are unable to differentiate to muscle cells owing to the lack of Baf60c (Albini et al., 2013).

ADP-ribosylation (ADPR) is a dynamic PTM, involving the transfer of ADP-ribose units from NAD^+ to specific amino acids or ADP-ribose itself with concomitant release of nicotinamide (Kraus, 2020). While the transfer of one ADP-ribose unit is called mono-ADPR or MARylation, the formation of a linear or branched chain is defined as poly-ADPR or PARylation (PAR) (Gibson and Kraus, 2012). ADPR is a fully reversible PTM, catalyzed by ADP-ribosyltransferases (Hottiger et al., 2010) and removed by ADPR hydrolases with different

[1]Department of Molecular Mechanisms of Disease, University of Zurich, Zurich, Switzerland

[2]Molecular Life Science PhD Program of the Life Science Zurich Graduate School, University of Zurich, Zurich, Switzerland

[3]Centre de Regulació Genomica (CRG), Barcelona Institute of Science and Technology (BIST), Dr. Aiguader 88, 08003 Barcelona, Spain

[4]Basic Sciences Department, Faculty of Medicine and Health Sciences, Universitat Internacional de Catalunya (UIC), 08003 Barcelona, Spain

[5]Sanford Burnham Prebys Medical Discovery Institute, La Jolla, CA, USA

[6]Universitat Pompeu Fabra (UPF), Barcelona, Spain

[7]Lead contact

*Correspondence: michael.hottiger@dmmd.uzh.ch

https://doi.org/10.1016/j.isci.2021.102432

subcellular localizations (Luscher et al., 2018). Among the nuclear enzymes responsible for ADPR catalysis, ARTD1 (also PARP1) is the best studied, mainly for its function in DNA damage response pathways and cancer progression (Azarm and Smith, 2020). ARTD1 activity is regulated by its flexible helical subdomain (HD), that in the properly folded status covers the NAD^+ pocket, while binding to DNA changes the protein conformation, thus unfolding the HD domain and allowing access of NAD^+ (Alemasova and Lavrik, 2019). In addition, activation of ARTD1 can be mediated by RNA (Kim et al., 2019) and regulated by other PTMs (Piao et al., 2014). Although the function of ARTD1 was intensively studied in the last decade, the mechanisms regulating its expression are poorly understood. While highly expressed in cancer cells, ARTD1 protein levels are rather low in noncancer cells as IMR90, skin fibroblasts, and hepatocytes (Chen et al., 2014). Its expression is regulated during cell cycle progression and cell-cycle arrest in G1 leads to the repression of *ARTD1* by binding of the HDAC-PRC2-SWI/SNF complex to its promoter and deposition of the repressive H3K27me3 histone mark (Wisnik et al., 2017; Pietrzak et al., 2018).

ADPR has been observed in several models of cell differentiation, either promoting or preventing the progression of differentiation depending on the context, timing, and NAD^+ availability (Abplanalp and Hottiger, 2017; Ryu et al., 2018). For instance, ADPR levels are modulated during adipogenesis to either repress or promote gene expression in different phases of the differentiation (Szanto and Bai, 2020) and application of the ADP-ribose chromatin-affinity purification method confirmed the enrichment of chromatin ADPR at promoters of PPARγ target genes during the later stage of adipogenesis (Bartolomei et al., 2016). Interestingly, the expression of *ARTD1* and its activity increased during reprogramming and depletion or inhibition of ARTD1 strongly decreased the efficiency of reprogramming (Chiou et al., 2013; Weber et al., 2013). Although ARTD1-dependent ADPR has been reported to play important roles in several differentiation and reprogramming pathways (Abplanalp and Hottiger, 2017), the existence and the contribution of ADPR during transdifferentiation was so far not investigated. In this study, we observed that MyoD-dependent transdifferentiation of fibroblasts to myoblasts induced nuclear ARTD1 levels and consequently increased nuclear ADPR that was catalyzed in a DNA damage-independent manner and was not associated to chromatin but rather localized to the nucleoplasm.

RESULTS

MyoD transdifferentiates IMR90 fibroblasts to myotubes

While ADPR was studied in several types of differentiation and reprogramming, its presence in transdifferentiation is so far still unknown. Thus, the MyoD-induced system was established, which has the unique property to allow distinguishing between the transdifferentiation step (i.e. cell type conversion) and the terminal differentiation (Dall'Agnese et al., 2019), allowing us to investigate ADPR specifically during transdifferentiation independently of its function in differentiation. The murine MyoD cDNA controlled by a doxycycline (dox)-inducible promoter was stably integrated into human IMR90 fibroblasts using the PiggyBac system (Dall'Agnese et al., 2019). IMR90 fibroblasts selected for the integrated MyoD construct ($MyoD^+$ fibroblasts) were subsequently treated with dox and the expression of MyoD was controlled by immunofluorescence (IF) microscopy. While MyoD was not detectable in untreated $MyoD^+$ fibroblasts, dox-treatment strongly induced its expression (Figure S1B). After MyoD-dependent transdifferentiation of human fibroblasts to myoblasts, these can be further differentiated to myotubes via serum deprivation (Figure S1A). The ability of the $MyoD^+$ myoblasts to further differentiate to myotubes was investigated by qPCR analysis of known myogenic markers such as *Myogenin*, *MyoD,* and *muscular creatine kinase*. Gene expression of untreated or dox-treated $MyoD^+$ cells after transdifferentiation (GM1) and either 1, 2, 3, or 5 days after induction of differentiation (DM1, DM2, DM3, DM5, respectively; Figures S1A and S1C) revealed that dox treatment and subsequent serum deprivation increased the expression of all three tested genes (Figure S1C). Because myotubes are multinucleated and characterized by high levels of myosin heavy chain (MHC), MHC expression was analyzed by IF at DM5. Differentiated $MyoD^+$ cells were multinucleated and expressed MHC in a dox-dependent manner (Figure S1D), confirming that the induction of MyoD successfully transdifferentiated IMR90 fibroblasts to committed myoblasts. To investigate ADPR exclusively during MyoD-dependent transdifferentiation, excluding its contribution to muscle differentiation, hereafter we exclusively focused on the first 24 h after dox treatment (GM1, Figure S1A).

MyoD induces *ARTD1* expression in transdifferentiated IMR90

Because ARTD1 participates in several differentiation and reprogramming systems (Abplanalp and Hottiger, 2017) but its contribution to transdifferentiation is unknown, we took advantage of the MyoD-induced transdifferentiation system to investigated its expression exclusively in transdifferentiated cells, thus

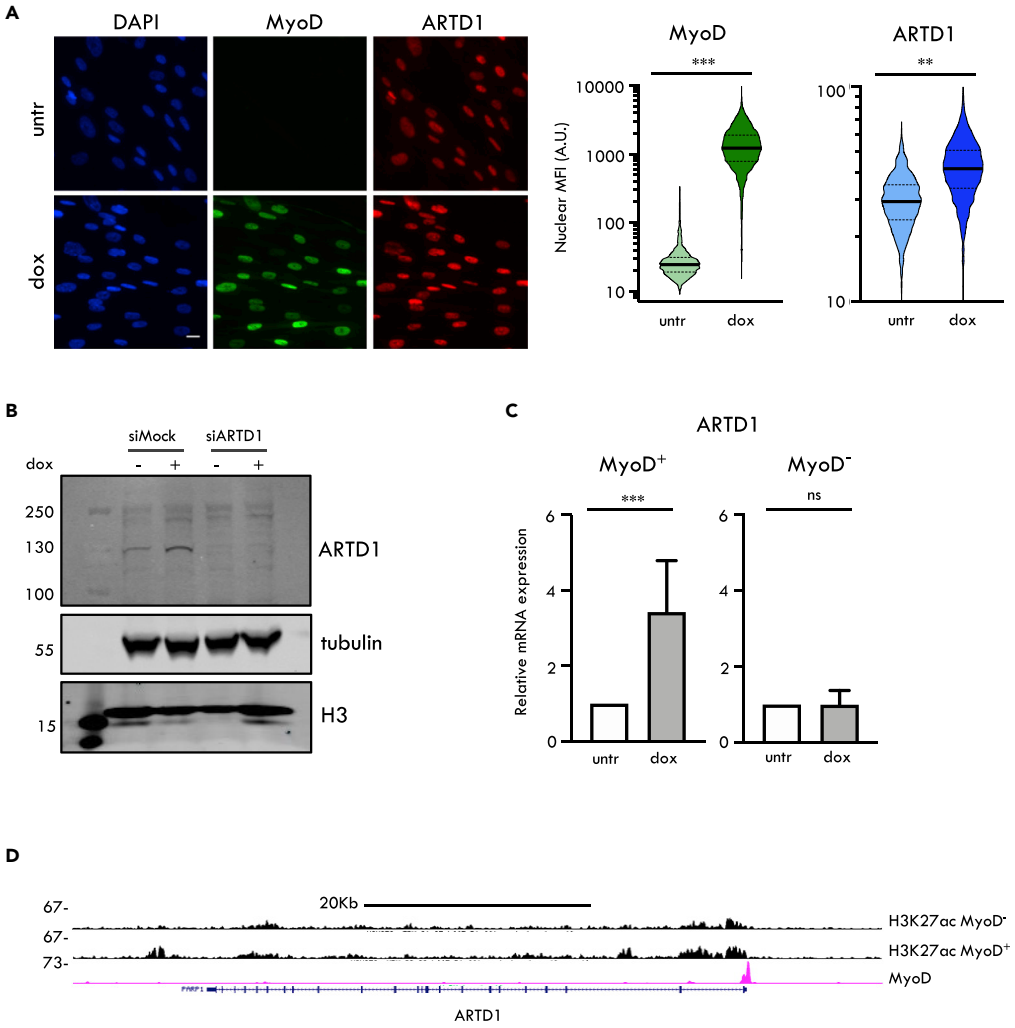

Figure 1. MyoD induces *ARTD1* expression in IMR90 cells

(A) IF of untreated (untr) or dox-treated (dox) MyoD$^+$ fibroblasts using anti-MyoD and anti-ARTD1 antibodies (magnification 20×). Scale bars indicate 20μm. Quantification on the right: the nuclear mean fluorescence intensity (arbitrary unit) of each event was normalized over the mean of the control/untreated, arbitrarily set to 30. The Y axes of violin plots are shown as log10 scales. For statistical analysis, a ratio-paired student t-test was used (n = 3–5; *, $p < 0.05$; **, $p < 0.005$; ***, $p < 0.0005$).

(B) WB analysis of untreated (dox -) or dox-treated (dox +) MyoD$^+$ fibroblasts upon siMock or siARTD1.

(C) qPCR for *ARTD1* in untreated (untr) or dox-treated (dox) MyoD$^+$ and MyoD$^-$ IMR90. Data are shown as mean ± SD. For statistical analysis, 3 to 5 independent experiments were compared using a ratio-paired student t-test with *, $p < 0.05$; **, $p < 0.005$; ***, $p < 0.0005$.

(D) UCSC browser showing MyoD binding (pink track) on human ARTD1 gene of MyoD$^+$ cells in GM1 and H3K27ac of MyoD$^-$ and MyoD$^+$ cells in GM1 (black tracks).

excluding its contribution to differentiation. MyoD$^+$ cells were treated with dox, and protein levels of both ARTD1 and MyoD were analyzed at the single-cell level by quantitative image-based cytometry (QIBC) (Toledo et al., 2013) (Figure 1A). In contrast to other reported systems, where the level of ARTD1 was easily detectable (Erener et al., 2012; Luo et al., 2017), it was weakly expressed in IMR90 fibroblasts and the dox-induced expression of MyoD significantly increased ARTD1 protein levels, as observed by IF but also by WB (Figures 1A and 1B), suggesting that MyoD might regulate the expression of *ARTD1*. Analysis of the *ARTD1* mRNA by qPCR indeed confirmed its increase in MyoD$^+$ cells upon dox-treatment. Conversely, control fibroblasts treated with dox (i.e. MyoD$^-$ cells) did not show any change in *ARTD1* levels, confirming that the observed increase of *ARTD1* is not a consequence of the dox treatment itself but is indeed

MyoD-dependent (Figure 1C). To test whether MyoD can directly bind the promoter of *ARTD1*, recently published ChIP-seq data of MyoD were analyzed (Dall'Agnese et al., 2019). MyoD binding was indeed observed at the proximal promoter of *ARTD1* in GM1 MyoD$^+$ cells (Figure 1D), suggesting that MyoD directly promotes *ARTD1* expression. Furthermore, the observed increased acetylation of histone 3 lysine 27 (H3K27ac) at the transcriptional start site of *ARTD1* in GM1 MyoD$^+$ cells confirmed the upregulation of *ARTD1* transcription in transdifferentiated cells.

To analyze whether the overexpression of MyoD is sufficient to increase ARTD1 levels in any cell line, we generated MyoD$^+$ HEK 293 cells and repeated the experiments. Despite the strong induction of MyoD upon dox treatment, ARTD1 level remained unchanged in MyoD$^+$ HEK 293 (Figures S2A and S2B), suggesting that the observed MyoD-dependent increase of ARTD1 is not ubiquitous. Furthermore, comparison of the basal (i.e. untreated) ARTD1 levels in IMR90 and HEK 293 cells revealed that ARTD1 levels were much lower in IMR90 cells (Figures S2B and 2C) (Chen et al., 2014), suggesting that the promoter of *ARTD1* is differently regulated in the two tested cell lines. qPCR analysis for myogenic markers in MyoD$^+$ HEK 293 cells treated with dox revealed that the overexpression of the murine MyoD did not activate the human myogenic program in this cell line (Figure S2D), confirming that not every cell line responds to MyoD-dependent cell conversion, most likely owing to the lack of MyoD cofactors (Choi et al., 1990; Skerjanc et al., 1994; Weintraub et al., 1989). Indeed, these results confirmed that the observed MyoD-dependent increase of *ARTD1* is not ubiquitous in every cell line but is rather specific of cells able to transdifferentiate.

ARTD1 does not contribute to MyoD-dependent regulation of chromatin compartmentalization

MyoD-induced transdifferentiation was described to be associated with an extensive three-dimensional (3D) reorganization of the genome via binding of MyoD to CTCF boundaries (Dall'Agnese et al., 2019). Because ARTD1 interacts with CTCF to regulate chromatin architecture (Zhao et al., 2015), we tested whether and to which extent ARTD1 would affect the chromatin compartmentalization during transdifferentiation. Hi-C analysis of untreated or dox-treated MyoD$^+$ cells confirmed that MyoD expression strongly altered A/B compartmentalization (Figure 2A, Table S1, S2). However, the eigenvector PCA analysis revealed that knockdown of ARTD1 only mildly affected A/B compartmentalization compared with the corresponding siMock control in both untreated and dox-treated MyoD$^+$ cells (Figure 2A), suggesting that the presence of ARTD1 has only a mild, local effect on A/B compartmentalization, however, in a transdifferentiation-independent manner.

Because knock down of ARTD1 does not allow distinguishing between the function of the protein and its enzymatic activity, the Hi-C analysis was repeated in presence of the PARP inhibitor Niraparib (PARPi) (Figure S3A). The samples treated with niraparib clustered slightly differently from the ones treated with siARTD1 (Figure S3A), suggesting that ARTD1 enzymatic activity might locally affect A/B compartmentalization but in a transdifferentiation-independent manner. Interestingly, cotreatment with niraparib and siARTD1 did not induce any additive changes to the knockdown of ARTD1 alone (Figure S3A), confirming that ARTD1 is the main ARTD family member contributing to A/B compartmentalization under the tested conditions. However, because both niraparib treatment and ARTD1 knockdown induced comparable changes in untreated as well as dox-treated cells, we concluded that the MyoD-induced ARTD1 and its enzymatic activity do not contribute to transdifferentiation by affecting the chromatin compartmentalization. This results also suggest that the newly transcribed, MyoD-dependent ARTD1 pool exerts a distinct function than the already present ARTD1 pool, indicating that functionally different ARTD1 pools can coexist at the same time.

ARTD1 mildly regulates the expression of a subset of MyoD-dependent genes

Because ARTD1 was described as transcription cofactor in several differentiation processes (Abplanalp and Hottiger, 2017), we tested whether it would coregulate MyoD-induced target genes. Therefore, RNA sequencing was performed on siMock MyoD$^+$ cells with or without dox treatment (siMock untreated *versus* siMock dox) and on dox-treated siARTD1 MyoD$^+$ cells (siARTD1 dox). The comparison of untreated *versus* dox-treated siMock MyoD$^+$ cells confirmed that MyoD strongly induces gene expression changes (Figure 2B) and gene ontology (GO) analysis confirmed that MyoD activated the myogenic program (Dall'Agnese et al., 2019) (Figure S3B). However, PCA analysis of the three samples revealed that while untreated and dox-treated MyoD$^+$ cells significantly differed from each other, the transcription profiles of cells transdifferentiated in presence or absence of ARTD1 were similar (Figure 2C, 2% variance). A more detailed

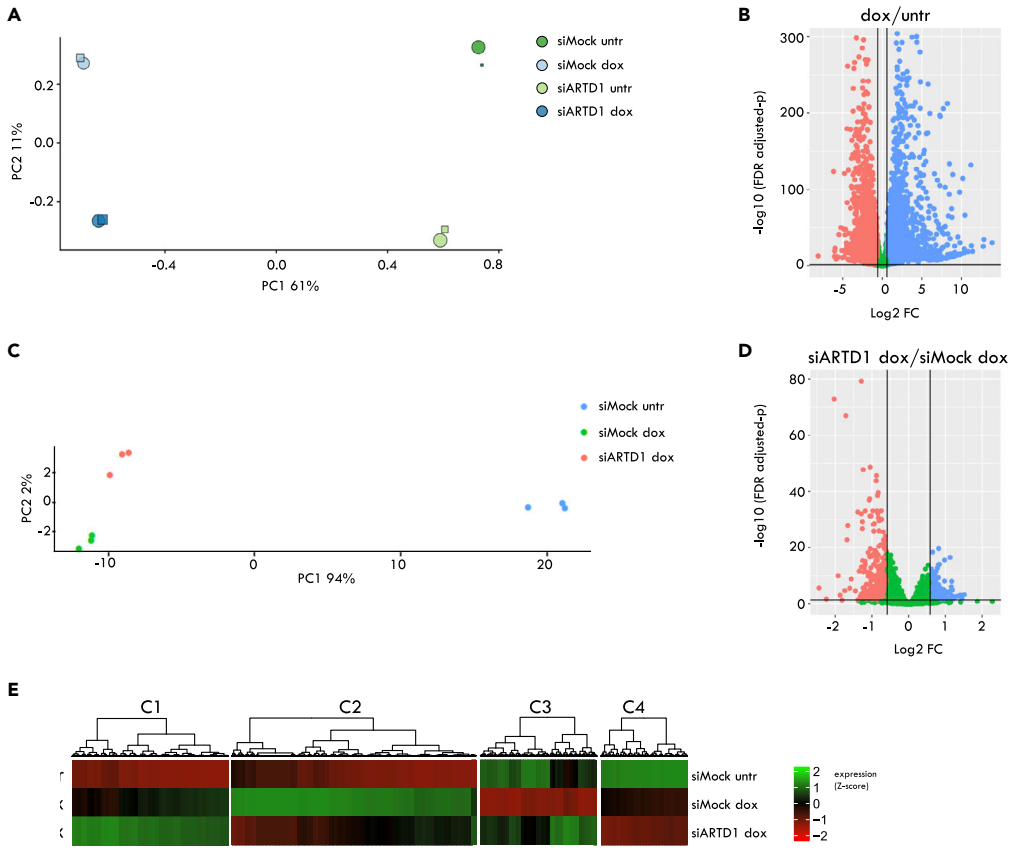

Figure 2. MyoD-dependent ARTD1 regulates gene expression of a subset of MyoD target genes

(A) PCA eigenvector analysis of changes in A/B compartmentalization of untreated and dox-treated MyoD$^+$ cells transfected with siMock or siARTD1 (shape indicates different batches; size indicates sequencing depth).

(B) Volcano plot showing the comparison of gene expression between untreated (untr) or dox-treated (dox) MyoD$^+$ fibroblasts. (Red dots: downregulated genes; Blue dots: upregulated genes; Green dots: unchanged genes; cutoff: fold change $\geq$1.5; p value on the y axes).

(C) PCA analysis showing the variation of gene expression between untreated and dox-treated MyoD$^+$ cells transfected with siMock or siARTD1 (each dot represents a biological replicate).

(D) Volcano plot showing the comparison of gene expression between dox-treated MyoD$^+$ fibroblasts transfected with either siARTD1 or siMock. (Red dots: downregulated genes; Blue dots: upregulated genes; Green dots: unchanged genes; cutoff: fold change $\geq$1.5; p value on the y axes).

(E) Heat map of differential gene expression between MyoD$^+$ cells untreated (untr), dox-treated (dox) transfected with either siMock or siARTD1 (cut-off: $\geq$ 2-fold difference between samples).

analysis of the differentially expressed genes of siMock dox and siARTD1 dox samples indicated that ARTD1 regulates the gene expression of a subset of upregulated as well as downregulated genes (Figure 2D). A heat map comparing the expression of genes differentially regulated in all the three samples allowed the identification of four clusters of genes (Figure 2E, Table S3: Deferentially regulated genes detected by RNAseq, Related to Figure 2). GO analysis of genes in cluster 1, whose expression was enhanced in absence of ARTD1, revealed that these genes were associated with general biological processes (e.g. cytoskeleton regulation and cell motility) (Figure S3C). GO analysis of genes in cluster 2 (the largest cluster, whose genes were induced by MyoD and showed reduced expression in absence of ARTD1) correlated with muscle differentiation and function (Figure S3D), genes of cluster 3 (that were repressed by MyoD but activated in absence of ARTD1) associated with different types of differentiation (e.g. chondrogenesis, osteogenesis, neurogenesis) (Figure S3E). Finally, GO analysis of genes in cluster 4 (that were repressed by MyoD and further reduced in absence of ARTD1) included inflammatory response genes, whose regulation by MyoD was reported before (Dall'Agnese et al., 2019) (Figure S3F). These results suggested that ARTD1 coregulates the expression of a small subset of MyoD target genes (304 genes, 8% of MyoD target genes,

Figure S3G), some of which favor transdifferentiation to myoblasts and prevent the induction of transdifferentiation to other cell types (i.e. clusters 2 and 3).

MyoD induces ARTD1-dependent nuclear ADP-ribosylation

To investigate whether MyoD-induced ARTD1 catalyzed PAR in transdifferentiated cells, the presence of PAR was assessed by QIBC in untreated and dox-treated MyoD$^+$ cells. Intriguingly, 24 h after dox treatment, we observed a significant increase of nuclear PAR (Figure 3A) that could also be detected with another anti-PAR antibody (Figure S4A). In dox-treated MyoD$^-$ cells, the basal nuclear PAR levels were barely detectable and did not change after dox treatment (Figure S4B), confirming that the increase of nuclear PAR was dependent on MyoD and was not a consequence of the dox treatment.

To strengthen that the MyoD-dependent nuclear PAR signal was enzymatically catalyzed, MyoD$^+$ cells were cotreated with dox and either Niraparib or Rucaparib, two different PARPi. Both inhibitors completely abolished the MyoD-dependent nuclear PAR (Figure 3B and S4C). To finally confirm that ARTD1 is the enzyme responsible for the observed PAR signal, ARTD1 was knocked down by siRNA in MyoD$^+$ cells, and these cells were subsequently treated with dox to induce transdifferentiation. As expected, knockdown of ARTD1 significantly reduced ARTD1 protein (Figure S4D) and, similar to the PARPi treatment, prevented the nuclear PAR accumulation (Figure 3C), confirming that ARTD1 is responsible for the PAR formation in transdifferentiation.

MyoD-induced nuclear ADP-ribosylation is dynamic and maintained in a MyoD-independent manner

Because continuous expression of MyoD is required to sustain transdifferentiation (Dall'Agnese et al., 2019), we tested whether the expression of ARTD1 and the accumulation of PAR would be reversible when the expression of MyoD is terminated by removing dox from the cells. Therefore, cells were transdifferentiated by dox treatment (GM1) and then dox was either maintained or removed for additional 24 or 48 h (GM2 and GM3, respectively). When dox was removed, the expression of MyoD drastically declined already within 24 h (GM2). Interestingly, neither ARTD1 nor nuclear PAR levels followed this drastic reduction but remained significantly higher as compared with untreated cells even 48 h after dox removal (Figure 3D), suggesting that after the initial induction by MyoD, the expression of *ARTD1* is regulated in a MyoD-independent manner. We therefore compared the expression of *ARTD1* and the MyoD target gene *Myogenin* after dox removal. Although MyoD binds the promoters of both genes after dox induction, the expression of *Myogenin* was immediately reduced after removal of dox, while *ARTD1* levels remained high even in absence of MyoD (Figures S4E and 4F), suggesting that once the expression of *ARTD1* is induced, MyoD is not further required. Moreover, this result suggested that MyoD-dependent ARTD1 might play a function in transdifferentiation that is not directly linked to the expression of the myogenic program but rather points toward a different function of ARTD1 in transdifferentiation.

ARTD1-induced PAR formation is very dynamic, and the half-life of the PAR is estimated to be within the minute range (Andersson et al., 2016). We thus investigated whether the PAR signal observed in absence of MyoD was continuously synthesized and degraded or rather stable. Therefore, MyoD$^+$ cells were treated with dox for 24 h (GM1) to induce ARTD1 and PAR and niraparib was added when dox was removed for additional 24 hr (GM2) (Figure 3E). While PAR levels were comparable in GM2 both in presence and absence of dox, niraparib treatment inhibited the nuclear PAR formation at GM2 (Figure 3E), suggesting that the nuclear PAR indeed undergoes continuous turnover, being synthesized by ARTD1 and likely degraded by an active nuclear PAR-eraser.

MyoD-dependent PAR synthesis is cell cycle independent and not induced by DNA damage

Because the activation of ARTD1 was linked to replication stress (Hanzlikova et al., 2018; Maya-Mendoza et al., 2018), we took advantage of the QIBC technology to analyze the distribution of PAR at the single-cell level and in a cell-cycle-dependent manner. The analysis confirmed that most of the IMR90 fibroblasts were accumulated in G1 phase before and after transdifferentiation (Figure S5A) (Dall'Agnese et al., 2019), however, cells with high or low PAR signals did not accumulate in any particular cell cycle phase (Figure S5B), thus excluding a functional contribution of MyoD-dependent PAR in cell cycle progression.

Alternatively, the activity of ARTD1 can be induced by damaged DNA (Azarm and Smith, 2020). We thus tested whether double-strand (ds) DNA breaks would activate ARTD1 during transdifferentiation. To

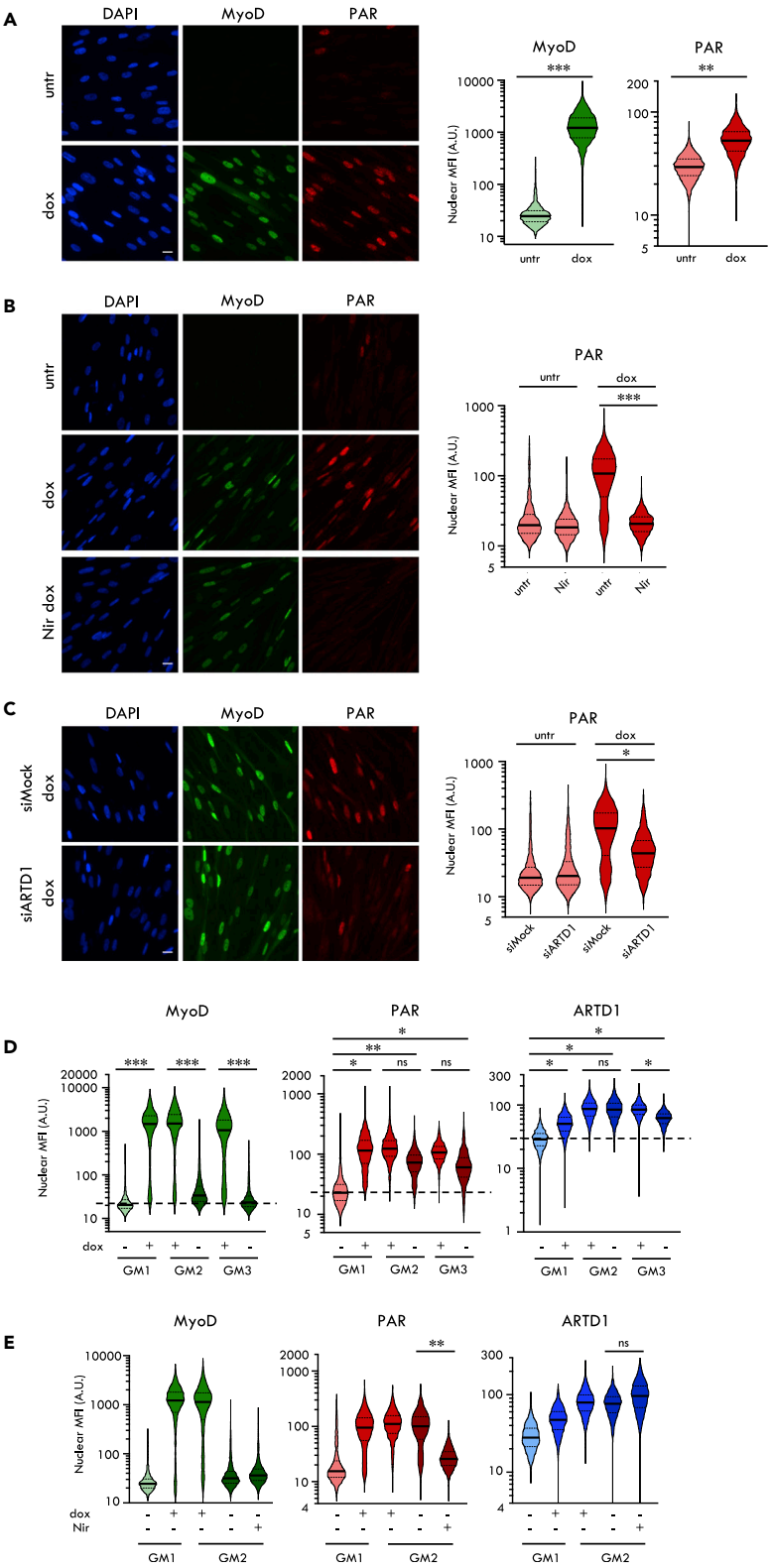

Figure 3. MyoD induces ARTD1-dependent nuclear ADP-ribosylation

(A) IF of untreated (untr) or dox-treated (dox) MyoD$^+$ fibroblasts using anti-MyoD and anti-PAR antibodies (magnification 20×). Scale bars indicate 20μm. Quantification on the right.

Figure 3. *Continued*

(B) IF of PARPi treatment of untreated or dox-treated MyoD$^+$ fibroblasts using anti MyoD and anti-PAR antibodies (Nir: niraparib, magnification 20×) Scale bars indicate 20μm. Quantification of PAR on the right.

(C) IF of untreated or dox-treated MyoD$^+$ fibroblasts upon siMock or siARTD1 transfection using anti-MyoD and anti-PAR antibodies (magnification 20×). Scale bars indicate 20μm. Quantification of PAR on the right.

(D) Quantification of the IF of MyoD$^+$ fibroblasts either untreated (untr) or dox-treated (dox) using anti-PAR and anti-MyoD antibodies. After 24h (GM1), dox was either maintained for additional 24 or 48 h (GM1 and GM2) or removed for the same time.

(E) Quantification of IF of MyoD$^+$ fibroblasts either untreated or dox-treated using anti-PAR, anti-MyoD and anti-ARTD1 antibodies. After 24 h (GM1), dox was either maintained for additional 24 h (GM2) or removed for the same time. Niraparib (Nir) was added at GM1 together with dox withdrawal (GM2 dox-, nir+). For every quantification, the IF signal was normalized as described in Figure 1. The Y axes of all violin plots are shown as log10 scales. For statistical analysis, a ratio-paired student t-test was used (n = 3-5; *, $p < 0.05$; **, $p < 0.005$; ***, $p < 0.0005$).

test whether dsDNA breaks would induce PAR formation, we analyzed the accumulation of γ-H2AX and 53BP1 foci upon transdifferentiation by QIBC including treatment with the topoisomerase II inhibitor etoposide as a positive control. As expected, in untreated IMR90, etoposide induced γ-H2AX mainly in cells allocated to the S-phase (Figure 4A). Interestingly, although a similar induction of γ-H2AX was observed in dox-treated cells without etoposide treatment, the high signal of γ-H2AX was again S-phase specific (Figure 4A), while cells with high MyoD-dependent PAR levels were equally distributed in all phases of the cell cycle (Figures 4B and S5B), suggesting that dsDNA breaks are unlikely responsible for the observed PAR formation. Moreover, dox treatment alone did not induce 53BP1 foci formation (Figure 4C), which was instead increased after the etoposide treatment (Figure 4C), providing further evidence that MyoD-dependent PAR is not induced by DNA damage but rather points to another yet to be defined mechanism that is peculiar of IMR90 cells.

Interestingly, although the levels of PAR were unchanged in transdifferentiated cells treated with etoposide (Figure 4D), they showed higher γ-H2AX and 53BP1 signals than untreated cells after etoposide treatment (Figures 4A and 4C), suggesting that the nuclear PAR accumulated during transdifferentiation might enhance the formation of γ-H2AX foci and thus the DNA damage response, for example by sustaining Nudix-dependent ATP production (Wright et al., 2016). To test whether the synthesized PAR would indeed be responsible for the sensitization of the transdifferentiated cells to genotoxic stress, we repeated the previously described experiments upon ARTD1 depletion. However, knock down of ARTD1 during transdifferentiation did not affect the enhanced etoposide-induced γ-H2AX and 53BP1 foci formation after dox treatment (Figures S5C and 5D), suggesting that the MyoD-dependent PAR itself is not responsible for the increased sensitivity to DNA damage in transdifferentiated cells.

MyoD-dependent ADP-ribosylation localizes to the nucleoplasm

To date, ARTD1-mediated PAR was associated to chromatin either contributing to DNA repair or regulating gene expression (Azarm and Smith, 2020; Luo et al., 2017; Hottiger, 2015). Because the MyoD-induced PAR was not involved in the regulation of the myogenic program and was not induced by DNA damage, we hypothesized that it might differ from the canonical one. When compared with H_2O_2-induced PAR, the signal intensity of the MyoD-dependent one was lower but detectable (Figure S6A). Interestingly, confocal microscopy revealed that the MyoD-dependent PAR signal displayed a different pattern profile in comparison with the H_2O_2-induced one, with big and round foci dispersed throughout the nucleus (Figure 5A).

Because histones are the main targets of ARTD1-mediated PAR upon H_2O_2 treatment (Gibbs-Seymour et al., 2016), we tested whether MyoD-induced PAR is associated to chromatin comparable with the described H_2O_2-induced one. Therefore, the chromatin association of PAR in untreated, dox-treated, or H_2O_2-treated MyoD$^+$ cells was examined by IF in combination with a pre-extraction step (Figures 5B and S6B). While H_2O_2-induced PAR was as expected strongly chromatin-associated after a mild (i.e. 0.1% Triton) or a more stringent pre-extraction treatment (i.e. 0.2% Triton), MyoD-dependent nuclear PAR was undetectable in both pre-extraction conditions (Figures 5B, S6B), suggesting that it is not associated to chromatin and probably does not serve the same function than chromatin-bound PAR. Costaining of PAR with two different histone marks, histone 3 lysine 4 methylation (H3K4me3) and histone 3 lysine 9 di-methylation (H3K9me2) revealed that MyoD-dependent nuclear PAR did not colocalize with either mark (Figure 5C), confirming that MyoD-induced PAR is rather localized to the nucleoplasm.

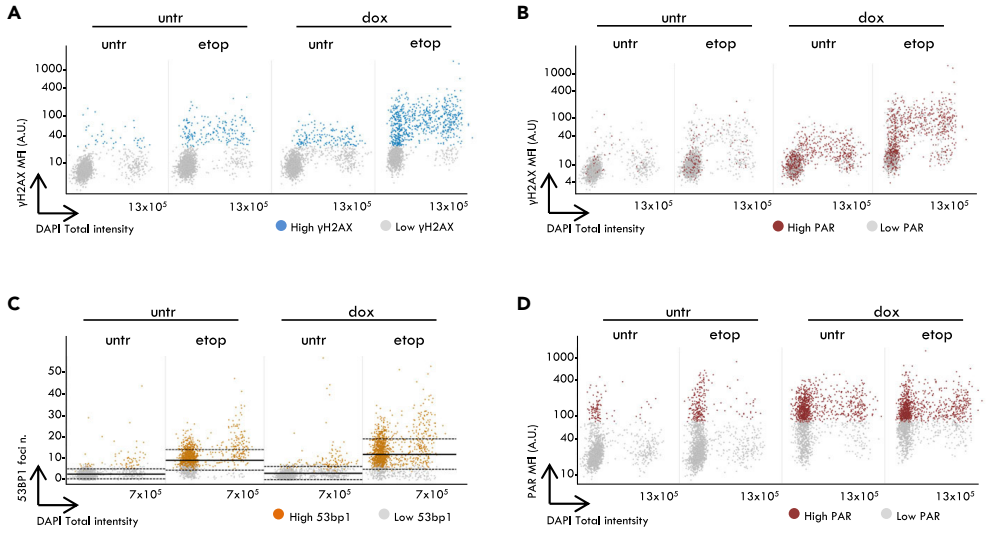

Figure 4. MyoD-dependent ADP-ribosylation is independent of dsDNA breaks

(A) γ-H2AX levels depicted as a function of cell cycle progression of untreated or dox-treated MyoD$^+$ cells, in presence of etoposide. Each dot represents a single cell. (Gray: low γ-H2AX; blue: high γ-H2AX).

(B) γ-H2AX levels depicted as a function of cell cycle progression and color-coded for nuclear PAR levels of untreated or dox-treated MyoD$^+$ cells, in presence of etoposide. Each dot represents a single cell (Gray: low PAR; red: high PAR).

(C) Nuclear 53BP1 foci depicted as a function of cell cycle progression of untreated or dox-treated MyoD$^+$ cells, in presence of etoposide. Each dot represents a single cell (Gray: low 53BP1; yellow: high 53BP1).

(D) Nuclear PAR levels depicted as a function of cell cycle progression of untreated or dox-treated MyoD$^+$ cells, in presence of etoposide. Each dot represents a single cell (Gray: low PAR; red: high PAR).

PARylation of ARTD1 was suggested to evict it from the chromatin (Muthurajan et al., 2014). To analyze the chromatin retention of ARTD1 during transdifferentiation, dox-treated cells were pre-extracted and analyzed by IF, using methanesulfonate (MMS) and olaparib cotreated cells as the positive control (Michelena et al., 2018). While MMS/olaparib induced a strong chromatin retention of ARTD1, transdifferentiation did not increase the affinity of ARTD1 for chromatin (Figures 5D, S6C). Moreover, as additional control, endogenous topoisomerase II was successfully detected on chromatin even after stringent pre-extraction (Figure S6D). Furthermore, chromatin fractionation followed by WB confirmed that ARTD1 is accumulated in the soluble fraction and does not associate to chromatin during transdifferentiation (Figure S6E). Altogether, these results revealed that the MyoD-induced ARTD1 indeed was not retained on chromatin and that MyoD-dependent PAR localized to the nucleoplasm, suggesting that automodification of ARTD1 might lead to its nucleoplasmic localization.

DISCUSSION

Although ARTD1 was described to coregulate several differentiation systems and cell reprogramming (Abplanalp and Hottiger, 2017), the contribution of ADPR to transdifferentiation is still unknown. Our results revealed that MyoD-dependent transdifferentiation induced ARTD1 expression, leading to increased nuclear PAR that was neither cell-cycle-dependent nor induced by DNA damage. MyoD-dependent nuclear PAR was highly dynamic being continuously synthesized and removed and unlike H_2O_2-induced PAR was not chromatin-bound but localized to the nucleoplasm.

Because we wanted to exclude the effect of the contribution of ARTD1 to further differentiation, the MyoD-dependent transdifferentiation of fibroblasts to myoblasts allowed us to focus exclusively on the transdifferentiation process (i.e. cell type conversion). In IMR90, MyoD bound to the promoter of *ARTD1* and increased its expression, leading to increased nuclear ARTD1 levels. This observation differed from what was shown for most of the studied differentiation systems where ARTD1 levels were rather stable or even decreased (Erener et al., 2012; Luo et al., 2017; Wisnik et al., 2017), pointing toward a new mechanism of regulating *ARTD1* expression in cellular plasticity. The MyoD-dependent increase of *ARTD1* was not observed when MyoD was overexpressed in HEK 293 cells, suggesting that cells unable to transdifferentiate (e.g. HEK293) do not show any increase of ARTD1 expression. This result might be explained by

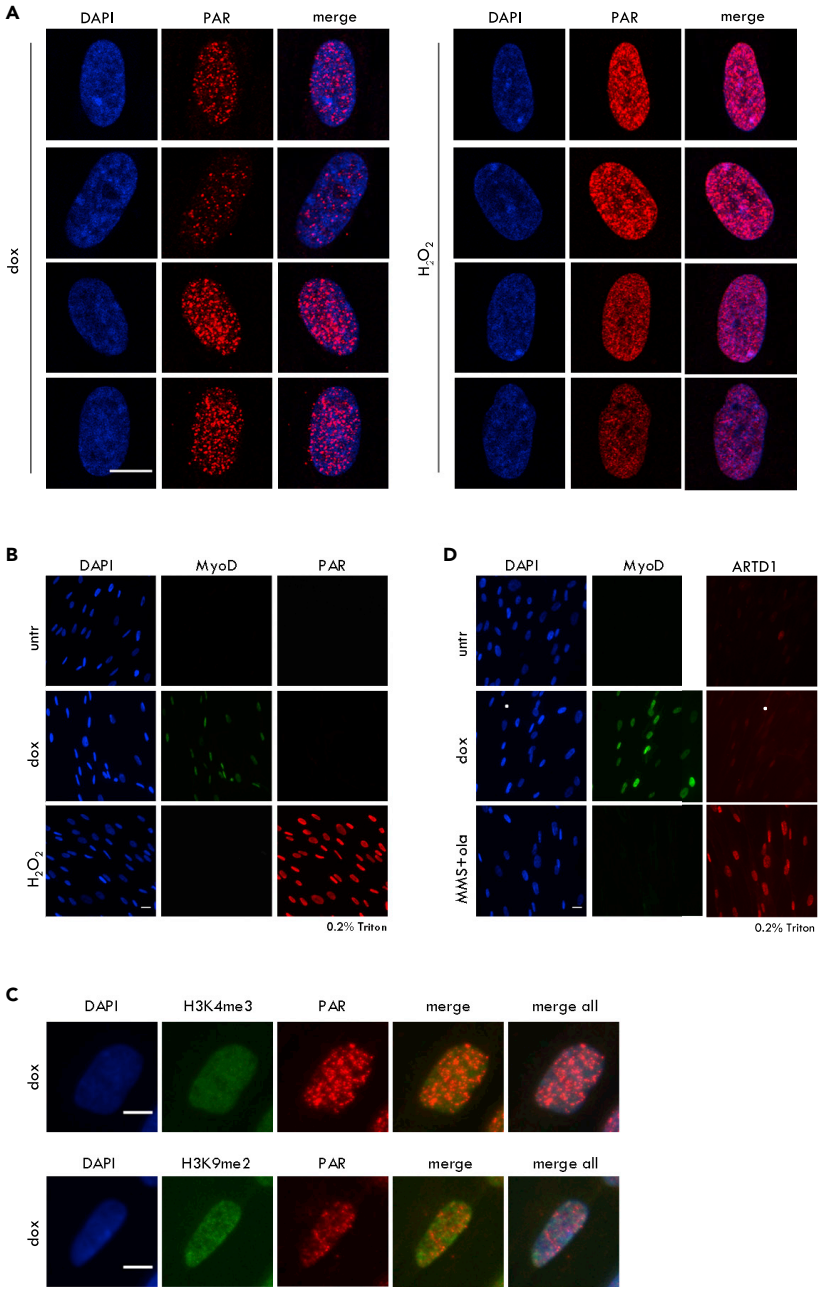

Figure 5. MyoD-dependent nuclear ADP-ribosylation localizes in foci that are not chromatin-bound

(A) Confocal pictures of dox-treated (dox) or H_2O_2-treated (H_2O_2) MyoD$^+$ fibroblasts stained with anti-PAR (zoom in of magnification 63×). Scale bars indicate 10 μm.

(B) IF for chromatin associated MyoD and PAR on MyoD$^+$ fibroblasts untreated or dox-treated or treated with H_2O_2 after pre-extraction with 0.2% Triton (magnification 20×). Scale bars indicate 20 μm.

(C) IF of dox-treated MyoD$^+$ fibroblasts using anti-H3K4me3 (upper panel), anti-H3K9me2 (lower panel) and anti-PAR antibodies (zoom in of magnification 20×) Scale bars indicate 10 μm.

(D) IF for chromatin associated MyoD and ARTD1 on MyoD$^+$ fibroblasts either untreated or dox-treated or co-treated with Methyl-methanesulfonate and Olaparib (MMS + Ola), after pre-extraction with 0.2% Triton (magnification 20×). Scale bars indicate 20 μm.

different chromatin landscapes in different cell lines. Interestingly, after transcriptional activation of the *ARTD1* gene, removal of MyoD only slightly reduced the *ARTD1* mRNA levels, while the expression of the canonical MyoD target gene *Myogenin* completely ceased, suggesting that the promoter region of *ARTD1* once activated, remains accessible and the gene is continuously expressed. The reason behind this different behavior of the promoters of ARTD1 and *Myogenin* in response to MyoD is so far still unknown, but this observed difference suggests that while *Myogenin* is essential for the activation of the myogenic program (Andres and Walsh, 1996), MyoD-induced ARTD1 has rather a different function in transdifferentiation.

The increased ARTD1 protein levels even 48 h after MyoD withdrawal cannot be explained with the stability of the protein because siRNA experiments revealed that ARTD1 protein is undetectable already 48 h after knockdown, indicating that ARTD1 has quite a short life span. Thus, we speculate that the ARTD1 expression is regulated by a positive feedback loop. We cannot exclude that a pool of ARTD1 might be in complex with other transcription factors than MyoD, regulating its own expression. Although the regulation of *ARTD1* transcription is not completely understood, several chromatin remodelers and transcription factors, such as Sp1, were described to modulate its expression (Zaniolo et al., 2005). MyoD recruits HATs and SWI/SNF and interacts with Sp1 (Tapscott, 2005). Thus, the expression of *ARTD1* might be regulated and maintained by a transcription factor that binds to the *ARTD1* promoter in a MyoD-dependent manner but then remains associated independently of MyoD.

Hi-C analysis during transdifferentiation revealed that MyoD is involved in chromatin rewiring at CTCF binding sites and MyoD-dependent changes in genome architecture are needed to activate the myogenic transcriptional program (Dall'Agnese et al., 2019). Moreover, CTCF was reported to be ADP-ribosylated by ARTD1 (Farrar et al., 2010) and interaction of ARTD1 and CTCF regulated the formation of Lamin-associated domains in a circadian-rhythm-dependent fashion (Zhao et al., 2015). Our Hi-C analysis confirmed that MyoD-dependent transdifferentiation led to strong changes in A/B compartmentalization, thus regulating the 3D genome architecture (Dall'Agnese et al., 2019). However, ARTD1 or its enzymatic activity had only a mild effect on A/B compartmentalization that was comparable both in fibroblasts and myoblasts, suggesting that the MyoD-dependent ARTD1 does not contribute to these changes.

The efficiency of transdifferentiation is very difficult to evaluate (Mills et al., 2019). An option to overcome this limitation is to compare transdifferentiated cells with normally differentiated ones. However, our current, dynamic envision of the epigenetic landscape rather suggests that cells changing their cellular identity by transdifferentiation use pathways that differ from the ones used for differentiation (Rajagopal and Stanger, 2016). Moreover, both transdifferentiation and differentiation are characterized by high levels of heterogeneity of chromatin landscapes and gene expression profiles, even between cells of the same population, thus making a comparison very difficult (Gulati et al., 2020). In this regard, although C2C12 myotubes and myotubes obtained from transdifferentiated IMR90 are globally comparable in terms of morphology and expression of myogenic markers, they are not identical because, for instance, they differ in the extent of ARTD1 expression and PAR formation (our own unpublished data). Our data rather point toward a different and distinct function of ARTD1 during differentiation and transdifferentiation. In this perspective, to investigate ARTD1's function in transdifferentiation by comparing transdifferentiated IMR90 with C2C12 would be very simplistic because the molecular pathway characterizing the two different types of myoblasts are very different. In addition, to dissect the role of ARTD1 in transdifferentiation by further differentiating MyoD-induced IMR90 to myotubes after ARTD1 knock down or inhibition would be inconclusive because ARTD1 is also involved in myogenesis (Olah et al., 2015) and to distinguish the function of ARTD1 for the initial cell type conversion versus its function during the subsequent differentiation would thus be very difficult. The best way to investigate ARTD1's contribution to MyoD-induced cell type conversion is to study fibroblasts to myoblasts transdifferentiation to focus exclusively on the initial step of the process. Our RNA-seq analysis during transdifferentiation confirmed the induction of the myogenic program. The number of MyoD target genes, whose expression was affected by ARTD1, was however quite small, and the loss of ARTD1 did not prevent overall transdifferentiation, suggesting that ARTD1 is dispensable for MyoD-dependent gene expression during transdifferentiation under the tested conditions. This is in line with the notion that MyoD alone is sufficient to activate the myogenic program (Sartorelli and Puri, 2018).

Although the enzymatic activity of ARTD1 is usually induced by replication stress or damaged DNA (Alemasova and Lavrik, 2019), the MyoD-dependent PAR formation was observed throughout the cell cycle

and was independent of dsDNA breaks. In line with this finding, basal ARTD1 activity was reported in different cancer cell lines in absence of DNA damage (Krukenberg et al., 2014), suggesting the existence of a different mechanism for ARTD1 activation that could be used also in transdifferentiated IMR90. Further experiments are required to elucidate the molecular mechanism responsible for the induction of the enzymatic activity of ARTD1 in MyoD-dependent transdifferentiation.

The current manuscript provides evidence that MyoD-induced PAR is not involved in regulation of gene expression, does not contribute to MyoD-dependent 3D chromatin architecture, is not induced by DNA damage, and does not contribute to cell cycle regulation. Unfortunately, we could not identify yet the function of MyoD-dependent PAR induction. However, our data revealed that MyoD-dependent ARTD1 and PAR were not associated to chromatin but localized to the nucleoplasm. In contrast to oxidative stress conditions, our pre-extraction experiments suggest that histones are very unlikely to be modified by MyoD-dependent ARTD1. Auto-ADPR of ARTD1 changes its physicochemical properties and chromatin affinity (Muthurajan et al., 2014). Thus, the present study suggests that the MyoD-dependent ARTD1 pool that is modified and localizes to the nucleoplasm is unlikely regulating any of the canonical, chromatin-linked functions (e.g. DNA repair or transcriptional regulation). This evidence rather suggests a so far undescribed function of PAR in the nucleoplasm. As HPF1 regulates ARTD1 specificity for histones as target proteins (Gibbs-Seymour et al., 2016), the lack of HPF1 or the expression of other cofactors might regulate the shift toward ARTD1 automodification and/or modification of other nucleoplasmic proteins. To investigate the ADP-ribosylome of IMR90 cells upon transdifferentiation, a special MS protocol is applied (Martello et al., 2016), which requires a large amount of starting material. IMR90 cells grow very slowly and do undergo senescence very quickly, thus not allowing to further investigate the ADP-ribosylome of transdifferentiated IMR90. In the nucleoplasm, PAR might recruit and regulate the local diffusion of nuclear proteins during transdifferentiation. Comparably, PAR mediates the shuttling of TARG between the nucleoli and the nucleoplasm after DNA damage (Butepage et al., 2018). Furthermore, owing to its negative charge, PAR behaves as a seeder of liquid-liquid demixing (Altmeyer et al., 2015). Thus, MyoD-dependent PAR foci might locally increase the concentration of PAR-binding proteins, allowing the establishment of membraneless nucleoplasmic environments with liquid-droplet-like behavior.

Transplantation of transdifferentiated cells, starting either with healthy donor cells or with genetically engineered patient fibroblasts, represents a potential therapeutic approach for several genetic diseases (Mollinari et al., 2018). Although, ARTD1-dependent PAR does not seem to contribute to transdifferentiation under the tested conditions, we speculate that it might increase its efficiency. However, single-cell RNA seq would be required to better investigate this hypothesis. Thus, further investigation of the function of ADPR in transdifferentiation might lead to the use of targeting ADPR (e.g. by inhibitors of the potential eraser) as possible therapeutic approach for genetic diseases.

Limitations of the study

The enzymatic activity of ARTD1 was induced during transdifferentiation in a cell cycle and DNA damage independent manner; however, the molecular mechanism behind ARTD1's activation remains elusive.

Moreover, although we observed that ARTD1-dependent PAR was not chromatin associated but localized to the nucleoplasm of transdifferentiated myoblasts, we could not identify the function of nuclear ADPR in the used system. Thus, the role of MyoD-dependent PAR is so far still unknown. Identifying which target proteins are modified by ARTD1 could help dissecting the molecular mechanism behind the increase of PAR after MyoD expression. Unfortunately, the used IMR90 cells proliferate slowly and quickly undergo senescence, thus not allowing to reach the required protein amounts to further investigate the ADP-ribosylome of transdifferentiated IMR90 cells.

It remains to be investigated to which extent the observed ARTD1-induced PAR can be also observed in other transdifferentiation systems.

Resource availability

Lead contact

michael.hottiger@dmmd.uzh.ch.

Materials availability

Plasmids and materials related to transdifferentiation should be requested to P. L. Puri (email address: lpuri@sbpdiscovery.org). All other materials are available from Michael O. Hottiger. This study did not generate any new unique reagent.

Data and code availability

All data is available in the main text or the supplementary information.

The Hi-C data and the RNA-seq data have been deposited in the NCBI database und ID BioProject: PRJNA610985.

METHODS

All methods can be found in the accompanying transparent methods supplemental file.

SUPPLEMENTAL INFORMATION

Supplemental information can be found online at https://doi.org/10.1016/j.isci.2021.102432.

ACKNOWLEDGMENTS

We thank Deena M. Leslie Pedrioli and Tobias Suter (University of Zurich) for providing editorial assistance. We thank the Center for Microscopy and Image Analysis (ZMB) and the Functional Genomics Center of the University of Zurich (FGCZ) for services and assistance. We especially thank Catharine Aquino from the FGCZ for helpful suggestions and discussions as well as technical support. PLP lab support from NIH/NIGMS (R01 GM134712-01), entitled "MYOD Regulation of 3D Chromatin Structure". Research in Beato's lab is supported by funds from the European Research Council under the European Union's Seventh Framework Program (FP7/2007-2013)/ERC Synergy grant agreement 609989 (4DGenome), from the Spanish Ministry of Economy and Competitiveness, 'Centro de Excelencia Severo Ochoa 2013-2017' and Plan Nacional (SAF2016-75006-P), as well as support of the CERCA Program/Generalitat de Catalunya. L.B was supported by the Forschungskredit 2019 of the University of Zurich and K.G by a grant of the Oncosuisse (Nr. KFS-3740-08-2015-R). ADP-ribosylation research in the laboratory of MOH is funded by the Kanton of Zurich and the Swiss National Science Foundation, Switzerland (grant 31003A_176177).

AUTHOR CONTRIBUTIONS

Project conceptualization and administration: M.O.H. and LB (lead).

Investigation: L.B. (lead), A-K.H., R.H.W., F.L.D., E.V., A.D., L.C., C.N. (supporting).

Methodology: L.B. (lead for the QIBC) and A-K.H. (supporting for the QIBC); R.H.W. and F.L.D (lead for the Hi-C) and L.B. (supporting); L.B. (lead for transdifferentiation establishment) and A.D. and P.L.P. (supporting).

Data curation and formal analysis: L.B. (lead), A-K.H. (supporting for the QIBC analysis); K.G. (lead for RNA-seq), L.B. (supporting); E.V.(lead for Hi-C), R.H.W. and F.L.D. and (supporting); L.C., C.N. and P.L.P. (lead for the ChIP-seq analysis) and L.B. (supporting).

Writing, review, and editing of MS: L.B. and M.O.H (lead), M.B., P.L.P. (supporting), A-K.H., R.H.W., F.L.D., K.G., A.D., L.C., C.N. (editing).

DECLARATION OF INTERESTS

The authors declare no financial interest.

Received: June 30, 2020
Revised: March 27, 2021
Accepted: April 11, 2021
Published: May 21, 2021

REFERENCES

Abplanalp, J., and Hottiger, M.O. (2017). Cell fate regulation by chromatin ADP-ribosylation. Semin. Cell Dev. Biol. *63*, 114–122.

Albini, S., Coutinho, P., Malecova, B., Giordani, L., Savchenko, A., Forcales, S.V., and Puri, P.L. (2013). Epigenetic reprogramming of human embryonic stem cells into skeletal muscle cells and generation of contractile myospheres. Cell Rep. *3*, 661–670.

Alemasova, E.E., and Lavrik, O.I. (2019). Poly(ADP-ribosyl)ation by PARP1: reaction mechanism and regulatory proteins. Nucleic Acids Res. *47*, 3811–3827.

Altmeyer, M., Neelsen, K.J., Teloni, F., Pozdnyakova, I., Pellegrino, S., Grofte, M., Rask, M.D., Streicher, W., Jungmichel, S., Nielsen, M.L., and Lukas, J. (2015). Liquid demixing of intrinsically disordered proteins is seeded by poly(ADP-ribose). Nat. Commun. *6*, 8088.

Andersson, A., Bluwstein, A., Kumar, N., Teloni, F., Traenkle, J., Baudis, M., Altmeyer, M., and Hottiger, M.O. (2016). PKCalpha and HMGB1 antagonistically control hydrogen peroxide-induced poly-ADP-ribose formation. Nucleic Acids Res. *44*, 7630–7645.

Andres, V., and Walsh, K. (1996). Myogenin expression, cell cycle withdrawal, and phenotypic differentiation are temporally separable events that precede cell fusion upon myogenesis. J. Cell Biol. *132*, 657–666.

Azarm, K., and Smith, S. (2020). Nuclear PARPs and genome integrity. Genes Dev. *34*, 285–301.

Bartolomei, G., Leutert, M., Manzo, M., Baubec, T., and Hottiger, M.O. (2016). Analysis of chromatin ADP-ribosylation at the genome-wide level and at specific loci by ADPr-ChAP. Mol. Cell *61*, 474–485.

Berkes, C.A., Bergstrom, D.A., Penn, B.H., Seaver, K.J., Knoepfler, P.S., and Tapscott, S.J. (2004). Pbx marks genes for activation by MyoD indicating a role for a homeodomain protein in establishing myogenic potential. Mol. Cell *14*, 465–477.

Butepage, M., Preisinger, C., von Kriegsheim, A., Scheufen, A., Lausberg, E., Li, J., Kappes, F., Feederle, R., Ernst, S., Eckei, L., et al. (2018). Nucleolar-nucleoplasmic shuttling of TARG1 and its control by DNA damage-induced poly-ADP-ribosylation and by nucleolar transcription. Sci. Rep. *8*, 6748.

Caretti, G., Di Padova, M., Micales, B., Lyons, G.E., and Sartorelli, V. (2004). The Polycomb Ezh2 methyltransferase regulates muscle gene expression and skeletal muscle differentiation. Genes Dev. *18*, 2627–2638.

Chen, H., Ruiz, P.D., Novikov, L., Casill, A.D., Park, J.W., and Gamble, M.J. (2014). MacroH2A1.1 and PARP-1 cooperate to regulate transcription by promoting CBP-mediated H2B acetylation. Nat. Struct. Mol. Biol. *21*, 981–989.

Chiou, S.H., Jiang, B.H., Yu, Y.L., Chou, S.J., Tsai, P.H., Chang, W.C., Chen, L.K., Chen, L.H., Chien, Y., and Chiou, G.Y. (2013). Poly(ADP-ribose) polymerase 1 regulates nuclear reprogramming and promotes iPSC generation without c-Myc. J. Exp. Med. *210*, 85–98.

Choi, J., Costa, M.L., Mermelstein, C.S., Chagas, C., Holtzer, S., and Holtzer, H. (1990). MyoD converts primary dermal fibroblasts, chondroblasts, smooth muscle, and retinal pigmented epithelial cells into striated mononucleated myoblasts and multinucleated myotubes. Proc. Natl. Acad. Sci. U S A *87*, 7988–7992.

Dall'Agnese, A., Caputo, L., Nicoletti, C., di Iulio, J., Schmitt, A., Gatto, S., Diao, Y., Ye, Z., Forcato, M., Perera, R., et al. (2019). Transcription factor-directed Re-wiring of chromatin architecture for somatic cell nuclear reprogramming toward trans-differentiation. Mol. Cell *76*, 453–472 e8.

Davis, R.L., Weintraub, H., and Lassar, A.B. (1987). Expression of a single transfected cDNA converts fibroblasts to myoblasts. Cell *51*, 987–1000.

de la Serna, I.L., Carlson, K.A., and Imbalzano, A.N. (2001). Mammalian SWI/SNF complexes promote MyoD-mediated muscle differentiation. Nat. Genet. *27*, 187–190.

Erener, S., Hesse, M., Kostadinova, R., and Hottiger, M.O. (2012). Poly(ADP-ribose) polymerase-1 (PARP1) controls adipogenic gene expression and adipocyte function. Mol. Endocrinol. *26*, 79–86.

Farrar, D., Rai, S., Chernukhin, I., Jagodic, M., Ito, Y., Yammine, S., Ohlsson, R., Murrell, A., and Klenova, E. (2010). Mutational analysis of the poly(ADP-ribosyl)ation sites of the transcription factor CTCF provides an insight into the mechanism of its regulation by poly(ADP-ribosyl) ation. Mol. Cell Biol. *30*, 1199–1216.

Gibbs-Seymour, I., Fontana, P., Rack, J.G.M., and Ahel, I. (2016). HPF1/C4orf27 is a PARP-1-interacting protein that regulates PARP-1 ADP-ribosylation activity. Mol. Cell *62*, 432–442.

Gibson, B.A., and Kraus, W.L. (2012). New insights into the molecular and cellular functions of poly(ADP-ribose) and PARPs. Nat. Rev. Mol. Cell Biol. *13*, 411–424.

Gulati, G.S., Sikandar, S.S., Wesche, D.J., Manjunath, A., Bharadwaj, A., Berger, M.J., Ilagan, F., Kuo, A.H., Hsieh, R.W., Cai, S., et al. (2020). Single-cell transcriptional diversity is a hallmark of developmental potential. Science *367*, 405–411.

Hanzlikova, H., Kalasova, I., Demin, A.A., Pennicott, L.E., Cihlarova, Z., and Caldecott, K.W. (2018). The importance of poly(ADP-ribose) polymerase as a sensor of unligated okazaki fragments during DNA replication. Mol. Cell *71*, 319–331 e3.

Hottiger, M.O. (2015). Nuclear ADP-ribosylation and its role in chromatin plasticity, cell differentiation, and epigenetics. Annu. Rev. Biochem. *84*, 227–263.

Hottiger, M.O., Hassa, P.O., Luscher, B., Schuler, H., and Koch-Nolte, F. (2010). Toward a unified nomenclature for mammalian ADP-ribosyltransferases. Trends Biochem. Sci. *35*, 208–219.

Ieda, M., Fu, J.D., Delgado-Olguin, P., Vedantham, V., Hayashi, Y., Bruneau, B.G., and Srivastava, D. (2010). Direct reprogramming of fibroblasts into functional cardiomyocytes by defined factors. Cell *142*, 375–386.

Kim, D.S., Camacho, C.V., Nagari, A., Malladi, V.S., Challa, S., and Kraus, W.L. (2019). Activation of PARP-1 by snoRNAs controls ribosome biogenesis and cell growth via the RNA helicase DDX21. Mol. Cell *75*, 1270–1285 e14.

Kraus, W.L. (2020). PARPs and ADP-ribosylation: 60 years on. Genes Dev. *34*, 251–253.

Krukenberg, K.A., Jiang, R., Steen, J.A., and Mitchison, T.J. (2014). Basal activity of a PARP1-NuA4 complex varies dramatically across cancer cell lines. Cell Rep. *8*, 1808–1818.

Luo, X., Ryu, K.W., Kim, D.S., Nandu, T., Medina, C.J., Gupte, R., Gibson, B.A., Soccio, R.E., Yu, Y., Gupta, R.K., and Kraus, W.L. (2017). PARP-1 controls the adipogenic transcriptional program by PARylating C/EBPbeta and modulating its transcriptional activity. Mol. Cell *65*, 260–271.

Luscher, B., Butepage, M., Eckei, L., Krieg, S., Verheugd, P., and Shilton, B.H. (2018). ADP-ribosylation, a multifaceted posttranslational modification involved in the control of cell physiology in health and disease. Chem. Rev. *118*, 1092–1136.

Martello, R., Leutert, M., Jungmichel, S., Bilan, V., Larsen, S.C., Young, C., Hottiger, M.O., and Nielsen, M.L. (2016). Proteome-wide identification of the endogenous ADP-ribosylome of mammalian cells and tissue. Nat. Commun. *7*, 12917.

Maves, L., Waskiewicz, A.J., Paul, B., Cao, Y., Tyler, A., Moens, C.B., and Tapscott, S.J. (2007). Pbx homeodomain proteins direct Myod activity to promote fast-muscle differentiation. Development *134*, 3371–3382.

Maya-Mendoza, A., Moudry, P., Merchut-Maya, J.M., Lee, M., Strauss, R., and Bartek, J. (2018). High speed of fork progression induces DNA replication stress and genomic instability. Nature *559*, 279–284.

Michelena, J., Lezaja, A., Teloni, F., Schmid, T., Imhof, R., and Altmeyer, M. (2018). Analysis of PARP inhibitor toxicity by multidimensional fluorescence microscopy reveals mechanisms of sensitivity and resistance. Nat. Commun. *9*, 2678.

Mills, J.C., Stanger, B.Z., and Sander, M. (2019). Nomenclature for cellular plasticity: are the terms as plastic as the cells themselves? EMBO J. *38*, e103148.

Mollinari, C., Zhao, J., Lupacchini, L., Garaci, E., Merlo, D., and Pei, G. (2018). Transdifferentiation: a new promise for neurodegenerative diseases. Cell Death Dis. *9*, 830.

Muthurajan, U.M., Hepler, M.R., Hieb, A.R., Clark, N.J., Kramer, M., Yao, T., and Luger, K. (2014). Automodification switches PARP-1 function from chromatin architectural protein to histone chaperone. Proc. Natl. Acad. Sci. U S A *111*, 12752–12757.

Olah, G., Szczesny, B., Brunyanszki, A., Lopez-Garcia, I.A., Gero, D., Radak, Z., and Szabo, C. (2015). Differentiation-associated downregulation of poly(ADP-ribose) polymerase-1 expression in myoblasts serves to increase their resistance to oxidative stress. PLoS One *10*, e0134227.

Patel, T., Tursun, B., Rahe, D.P., and Hobert, O. (2012). Removal of Polycomb repressive complex 2 makes C. elegans germ cells susceptible to direct conversion into specific somatic cell types. Cell Rep. *2*, 1178–1186.

Piao, L., Kang, D., Suzuki, T., Masuda, A., Dohmae, N., Nakamura, Y., and Hamamoto, R. (2014). The histone methyltransferase SMYD2 methylates PARP1 and promotes poly(ADP-ribosyl)ation activity in cancer cells. Neoplasia *16*, 257–264, 64 e2.

Pietrzak, J., Spickett, C.M., Ploszaj, T., Virag, L., and Robaszkiewicz, A. (2018). PARP1 promoter links cell cycle progression with adaptation to oxidative environment. Redox Biol. *18*, 1–5.

Rajagopal, J., and Stanger, B.Z. (2016). Plasticity in the adult: how should the waddington diagram Be applied to regenerating tissues? Dev. Cell *36*, 133–137.

Ryu, K.W., Nandu, T., Kim, J., Challa, S., DeBerardinis, R.J., and Kraus, W.L. (2018). Metabolic Regulation of Transcription through Compartmentalized NAD(+) Biosynthesis. Science *360*, eaan5780.

Sartorelli, V., and Puri, P.L. (2018). Shaping gene expression by landscaping chromatin architecture: lessons from a master. Mol. Cell *71*, 375–388.

Skerjanc, I.S., Slack, R.S., and McBurney, M.W. (1994). Cellular aggregation enhances MyoD-directed skeletal myogenesis in embryonal carcinoma cells. Mol. Cell Biol. *14*, 8451–8459.

Szanto, M., and Bai, P. (2020). The role of ADP-ribose metabolism in metabolic regulation, adipose tissue differentiation, and metabolism. Genes Dev. *34*, 321–340.

Tapscott, S.J. (2005). The circuitry of a master switch: myod and the regulation of skeletal muscle gene transcription. Development *132*, 2685–2695.

Toledo, L.I., Altmeyer, M., Rask, M.B., Lukas, C., Larsen, D.H., Povlsen, L.K., Bekker-Jensen, S., Mailand, N., Bartek, J., and Lukas, J. (2013). ATR prohibits replication catastrophe by preventing global exhaustion of RPA. Cell *155*, 1088–1103.

Weber, F.A., Bartolomei, G., Hottiger, M.O., and Cinelli, P. (2013). Artd1/Parp1 regulates reprogramming by transcriptional regulation of Fgf4 via Sox2 ADP-ribosylation. Stem Cells *31*, 2364–2373.

Weintraub, H., Tapscott, S.J., Davis, R.L., Thayer, M.J., Adam, M.A., Lassar, A.B., and Miller, A.D. (1989). Activation of muscle-specific genes in pigment, nerve, fat, liver, and fibroblast cell lines by forced expression of MyoD. Proc. Natl. Acad. Sci. U S A *86*, 5434–5438.

Wisnik, E., Ploszaj, T., and Robaszkiewicz, A. (2017). Downregulation of PARP1 transcription by promoter-associated E2F4-RBL2-HDAC1-BRM complex contributes to repression of pluripotency stem cell factors in human monocytes. Sci. Rep. *7*, 9483.

Wright, R.H., Lioutas, A., Le Dily, F., Soronellas, D., Pohl, A., Bonet, J., Nacht, A.S., Samino, S., Font-Mateu, J., Vicent, G.P., et al. (2016). ADP-ribose-derived nuclear ATP synthesis by NUDIX5 is required for chromatin remodeling. Science *352*, 1221–1225.

Zaniolo, Karine, Rufiange, Anne, Leclerc, Steeve, Desnoyers, Serge, and Guérin, Sylvain (2005). Regulation of the poly(ADP-ribose) polymerase-1 gene expression by the transcription factors Sp1 and Sp3 is under the influence of cell density in primary cultured cells. Biochem. J. *389*, 423–433.

Zhao, H., Sifakis, E.G., Sumida, N., Millan-Arino, L., Scholz, B.A., Svensson, J.P., Chen, X., Ronnegren, A.L., Mallet de Lima, C.D., Varnoosfaderani, F.S., et al. (2015). PARP1- and CTCF-mediated interactions between active and repressed chromatin at the lamina promote oscillating transcription. Mol. Cell *59*, 984–997.

iScience, Volume *24*

Supplemental information

MyoD induces ARTD1 and nucleoplasmic poly-ADP-ribosylation during fibroblast to myoblast transdifferentiation

Lavinia Bisceglie, Ann-Katrin Hopp, Kapila Gunasekera, Roni H. Wright, François Le Dily, Enrique Vidal, Alessandra Dall'Agnese, Luca Caputo, Chiara Nicoletti, Pier Lorenzo Puri, Miguel Beato, and Michael O. Hottiger

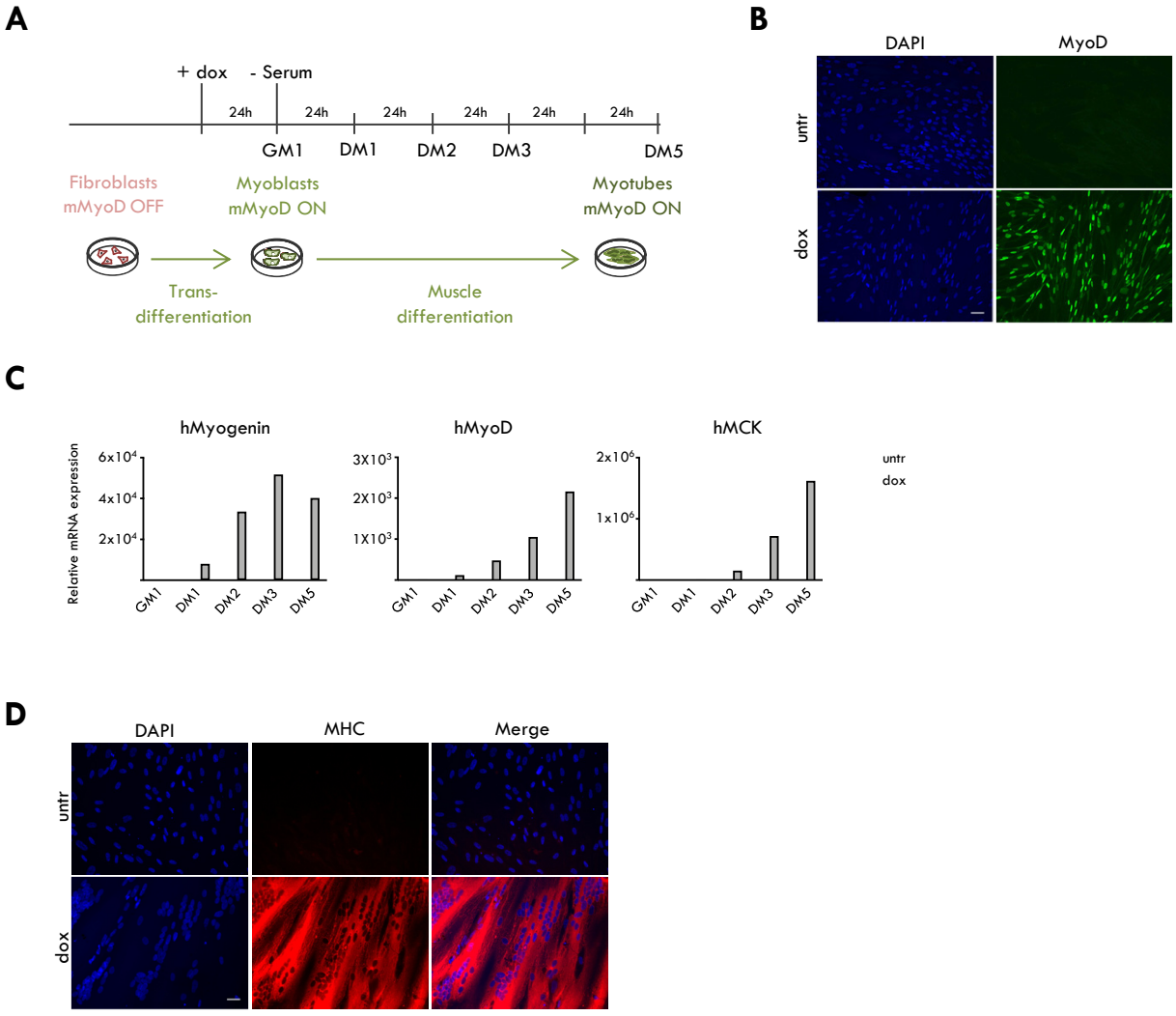

Suppl. Figure 1: MyoD induction converts IMR90 fibroblasts into myotubes. Related to Figure 1. **(A)** Scheme representing the trans-differentiation protocol: 24h treatment with doxycycline (dox) induces MyoD expression, thus converting fibroblasts into myoblasts (GM1 condition: 24h of Growth Medium with dox). Myoblasts are differentiated into myotubes by serum removal for several days (DM1, DM2, DM3, DM5 = 1, 2, 3 or 5 days in Differentiation Medium). **(B)** IF of MyoD$^+$ fibroblasts with or without dox using anti MyoD antibody (magnification 20x). Scale bars indicate 50 µm. **(C)** qPCR for human myogenic markers *Myogenin*, *MyoD* and *Muscular Creatin Kinase* (MCK) on MyoD$^+$ IMR90 (GM1, DM1, 2, 3, 5). **(D)** IF staining of MyoD$^+$ fibroblasts using with Myosin Heavy Chain (MHC) antibody (magnification 20x). Scale bars indicate 50 µm.

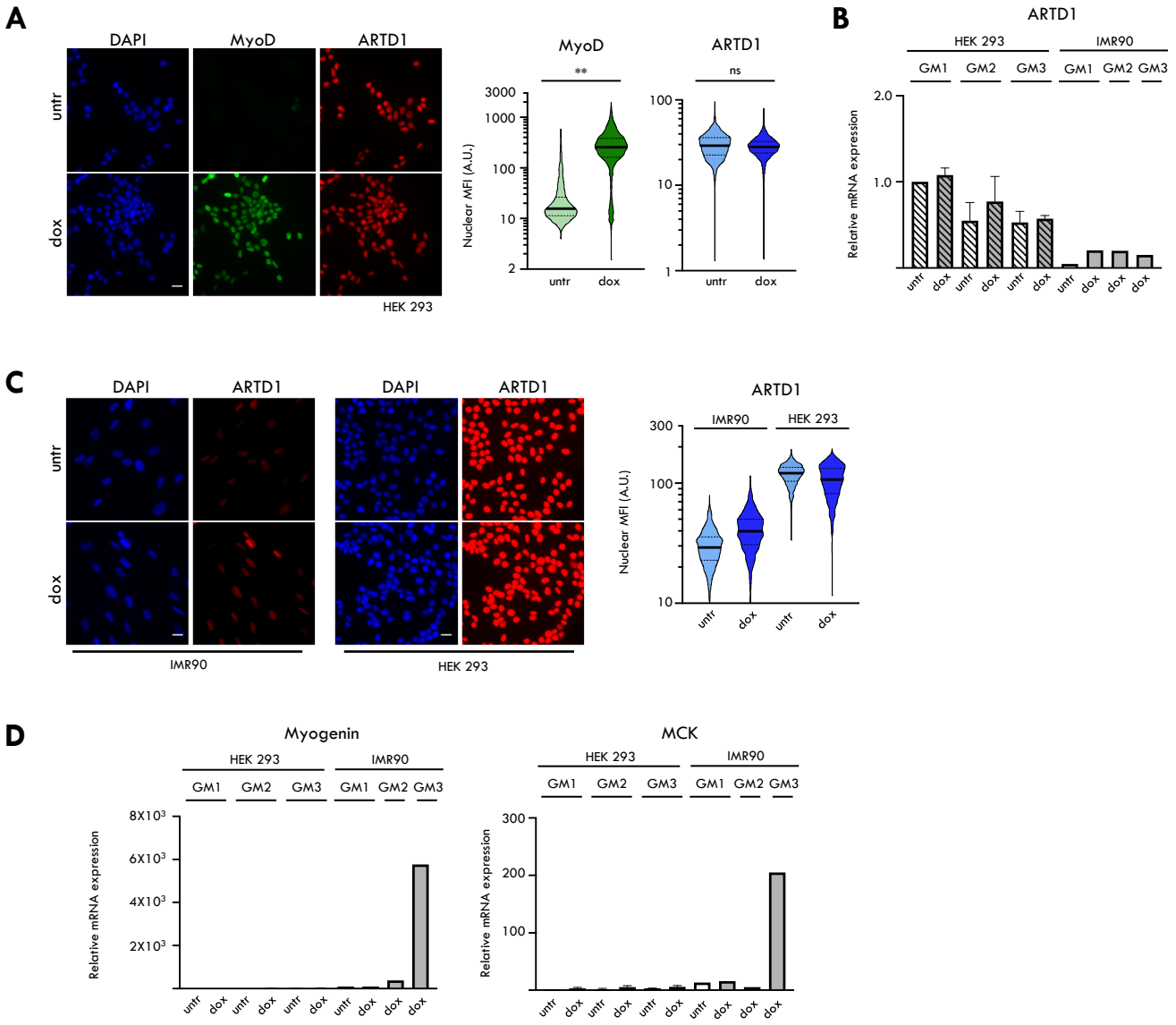

Suppl. Figure 2: MyoD does not induce *ARTD1* expression in HEK293 cells. Related to Figure 1. **(A)** IF of HEK 293 cells using anti-ARTD1 and anti-MyoD antibodies (magnification 20x). Quantification on the right. Scale bars indicate 20 µm. **(B)** qPCR for ARTD1 in HEK 293 and IMR90 cells untreated (untr) or dox-treated (dox) for 24 (GM1), 48 (GM2) or 72 hours (GM3). Data are shown as Mean +/- SD **(C)** IF of untreated (untr) or dox-treated (dox) IMR90 and HEK 293 cells using anti-ARTD1 antibody (magnification 20x). Scale bars indicate 20 µm. Quantification on the right. **(D)** qPCR for ARTD1 and human myogenic markers in HEK 293 and IMR90 cells untreated (untr) or dox-treated (dox) for 24 (GM1), 48 (GM2) or 72 hours (GM3). Data are shown as Mean +/- SD.
For every quantification, the IF signal was normalised as described in Figure 1. The Y-axes of all violin plots are shown as log10 scales. For statistical analysis, a ratio-paired student t-test was used (n =3-5; *, $p<0.05$; **, $p<0.005$; ***, $p < 0.0005$).

A

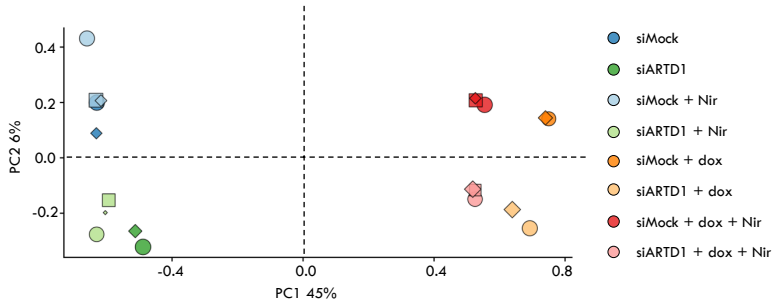

B

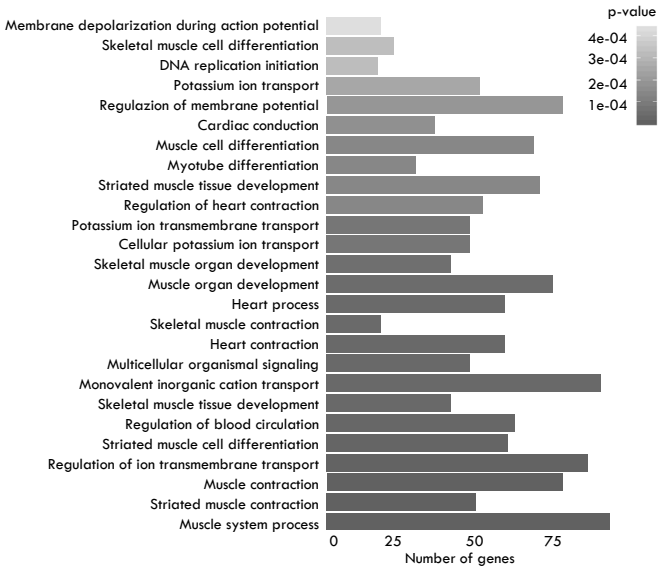

C

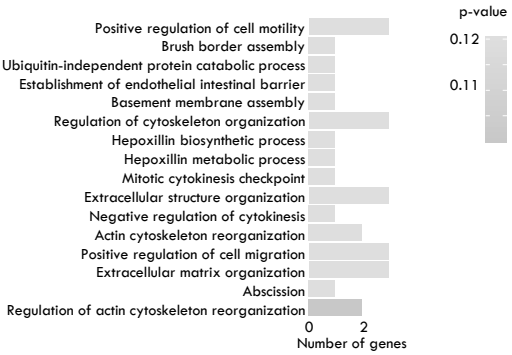

D

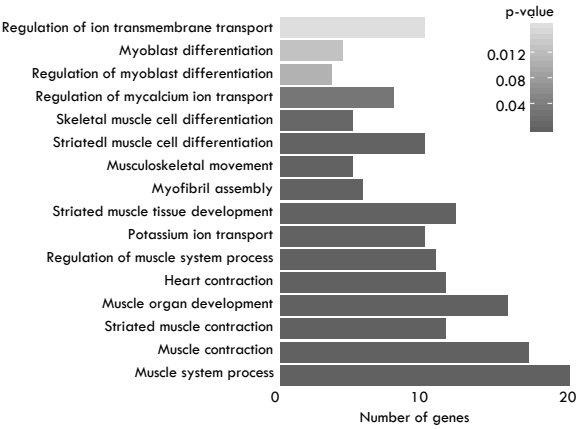

E

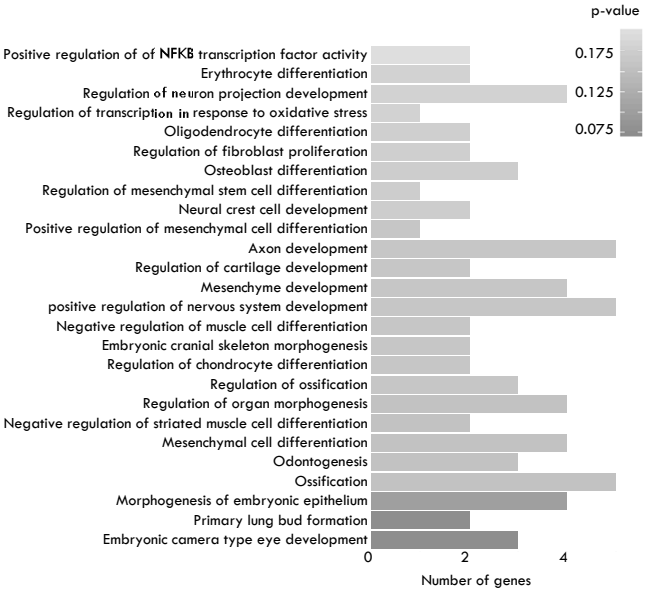

F

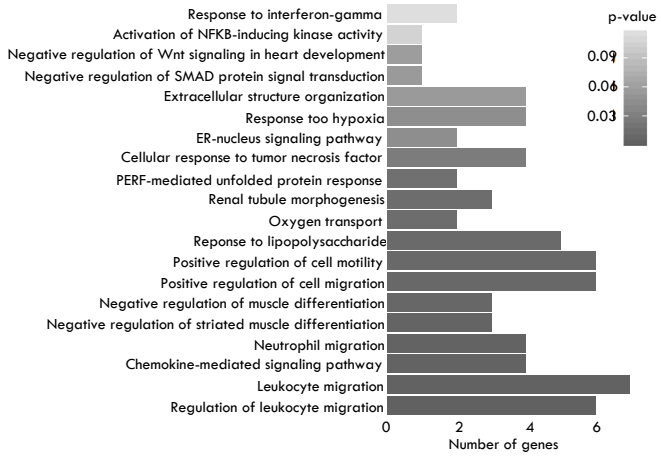

G

SiMock untr	SiMock Dox	SiARTD1 dox	
18328	2033	14	C1
		205	C2
	1709	56	C3
		29	C4

Suppl. Figure 3: ARTD1 regulates only a subset of MyoD target genes involved in cell type conversion. Related to Figure 2.

(A) PCA eigenvector analysis of changes in A/B compartmentalization in untreated and dox-treated $MyoD^+$ cells transfected with siMock or siARTD1 and treated with Niraparib (shape indicates different batches; size indicates sequencing depth). **(B)** GO analysis of genes up-regulated in siMock dox compared to siMock untreated **(C)** GO analysis of cluster 1. **(D)** GO analysis of cluster 2. **(E)** GO analysis of cluster 3. **(F)** GO analysis of cluster 4. **(G)** Number of transcripts with differential expression for each condition. siMock untr versus siMock dox: cut-off ≥ 2-fold change, p-value < 0.05; siMock dox versus siARTD1 dox: cut-off ≥ 1.5-fold change, p-value < 0.05.

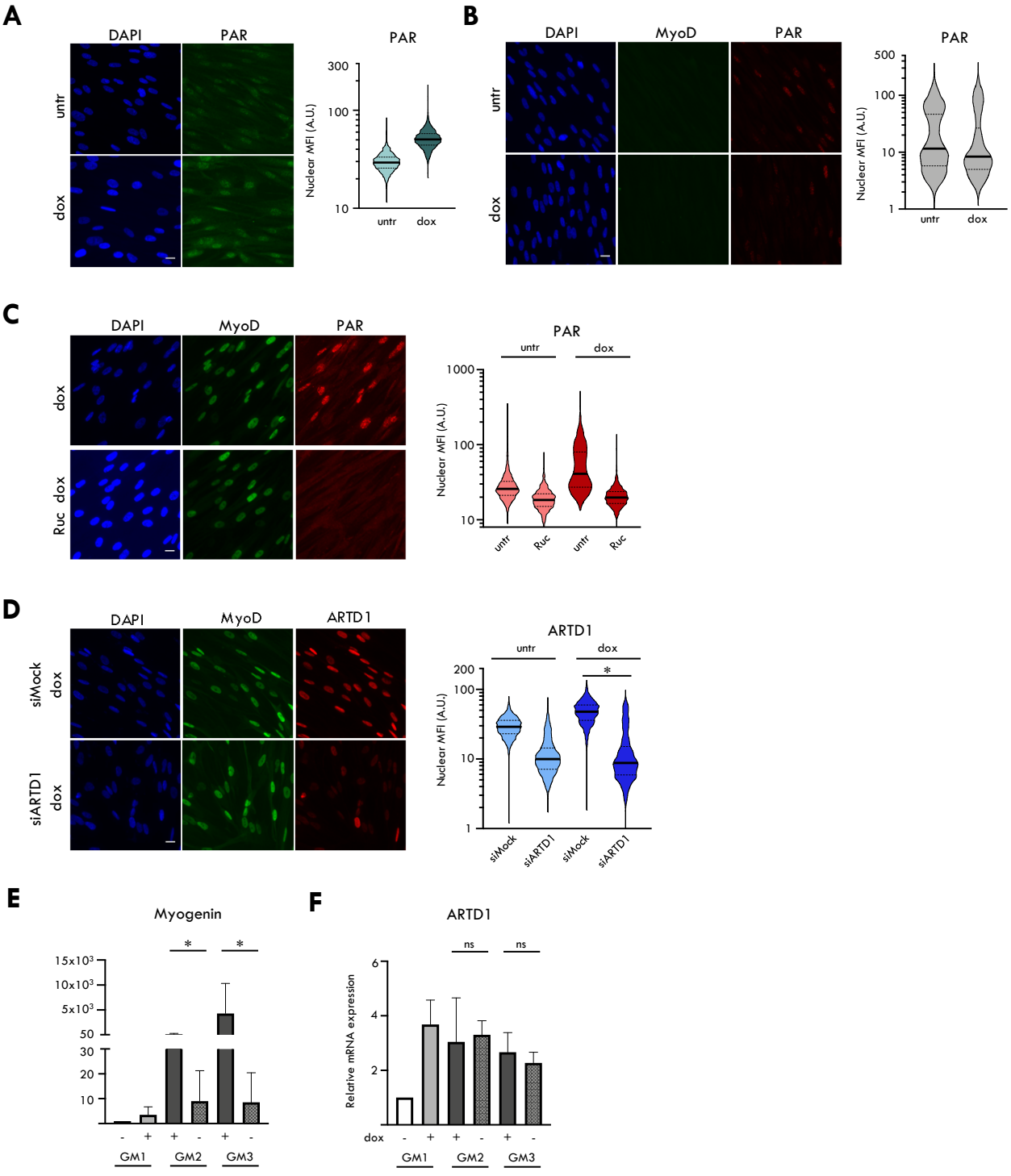
A
DAPI
PAR
untr
dox
PAR
Nuclear MFI (A.U.)
300
100
10
untr
dox
B
DAPI
MyoD
PAR
untr
dox
PAR
Nuclear MFI (A.U.)
500
100
10
1
untr
dox
C
DAPI
MyoD
PAR
dox
Ruc dox
PAR
untr
dox
Nuclear MFI (A.U.)
1000
100
10
untr
Ruc
untr
Ruc
D
DAPI
MyoD
ARTD1
siMock
dox
siARTD1
dox
ARTD1
untr
dox
*
Nuclear MFI (A.U.)
200
100
10
1
siMock
siARTD1
siMock
siARTD1
E
Myogenin
*
*
15x10³
10x10³
5x10³
50
30
20
10
- + + - + -
GM1
GM2
GM3
F
ARTD1
ns
ns
Relative mRNA expression
6
4
2
dox - + + - + -
GM1
GM2
GM3

Suppl. Figure 4: PARPi treatment and knock-down of ARTD1 inhibit the MyoD-dependent nuclear PAR. Related to Figure 3.

(A) IF of untreated (untr) or dox-treated (dox) $MyoD^+$ fibroblasts using anti-PAR (Abcam) (magnification 20x). Scale bars indicate 20 μm. Quantification on the right. **(B)** IF of untreated or dox-treated control $MyoD^-$ fibroblasts using anti-MyoD and anti-PAR antibodies (magnification 20x). Scale bars indicate 20 μm. Quantification of PAR on the right. **(C)** IF of untreated (untr) or dox-treated (dox) $MyoD^+$ fibroblasts upon PARPi Rucaparib (Ruc) using anti MyoD and anti-PAR antibodies (magnification 20x). Scale bars indicate 20 μm. Quantification of PAR on the right. **(D)** IF of untreated or dox-treated $MyoD^+$ fibroblasts upon siMock or siARTD1 using anti-MyoD and anti-ARTD1 antibodies (magnification 20x). Scale bars indicate 20 μm. Quantification of ARTD1 on the right. **(E/F)** qPCR for *Myogenin* and *ARTD1* in untreated or dox-treated $MyoD^+$ IMR90. After 24 hours (GM1) dox was either maintained for additional 24, or 48 hours (GM2 and GM3) or removed for the same time. Data are shown as Mean +/- SD. For statistical analysis, 3 to 5 independent experiments were compared using a ratio-paired student t-test with *, $p<0.05$; **, $p<0.005$; ***, $p < 0.0005$.

For every quantification, the IF signal was normalised as described in Figure 1. The Y-axes of all violin plots are shown as log10 scales. For statistical analysis, a ratio-paired student t-test was used (n =3-5; *, $p<0.05$; **, $p<0.005$; ***, $p < 0.0005$).

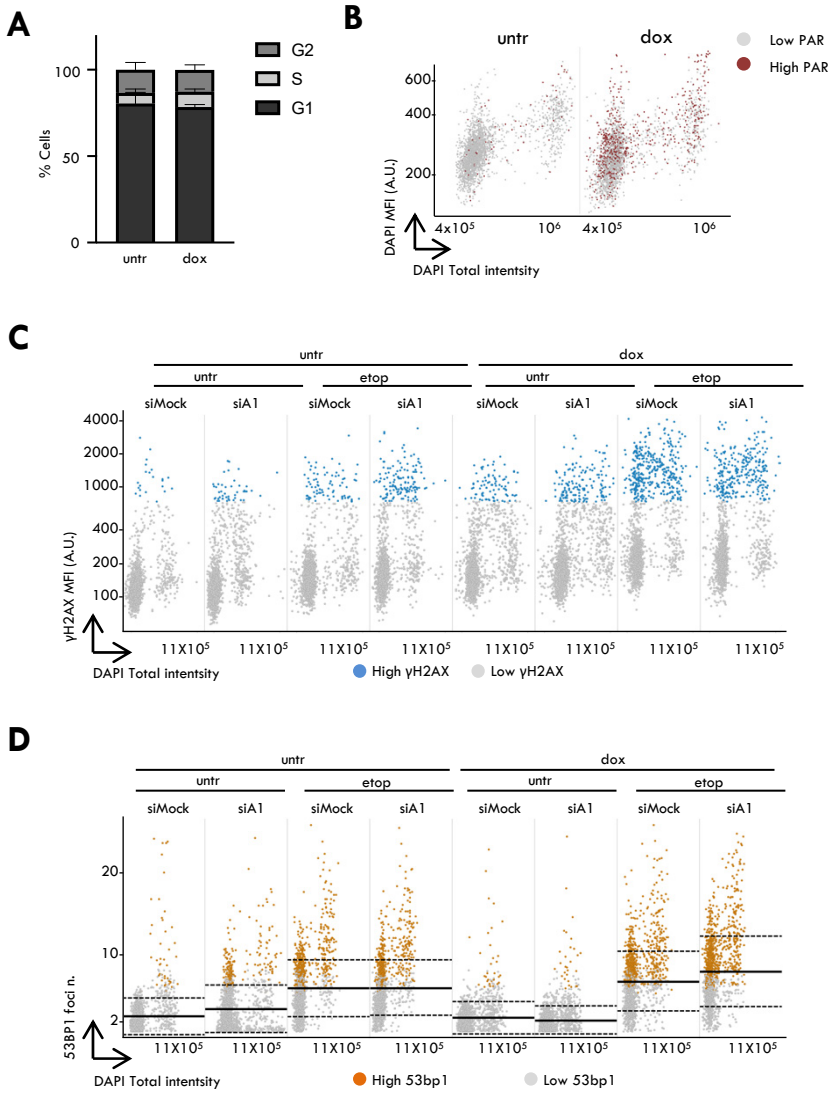

Suppl. Figure 5: Trans-differentiation increases etoposide sensitivity of IMR90 independently of ARTD1. Related to Figure 4.

(A) Cell-cycle distribution of untreated or dox-treated MyoD$^+$ fibroblasts. Data are shown as percentage of cells +/- SD. **(B)** Untreated or dox-treated MyoD$^+$ fibroblasts stained with anti-PAR antibody. Total versus mean DAPI intensities color-coded for PAR depicted as a function of cell cycle progression. (Grey dots: low PAR; red dots: high PAR). **(C)** γ-H2AX levels depicted as a function of cell cycle progression in untreated or dox-treated MyoD$^+$ cells, transfected with siMock or siARTD1 and in presence of etoposide. Each dot represents a single cell. **(**Grey: low γ-H2AX; blue: high γ-H2AX). **(D)** 53BP1 levels depicted as a function of cell cycle progression in untreated or dox-treated MyoD$^+$ cells, transfected with siMock or siARTD1 and in presence of etoposide. Each dot represents a single cell. **(**Grey: low 53BP1; orange: high 53BP1).

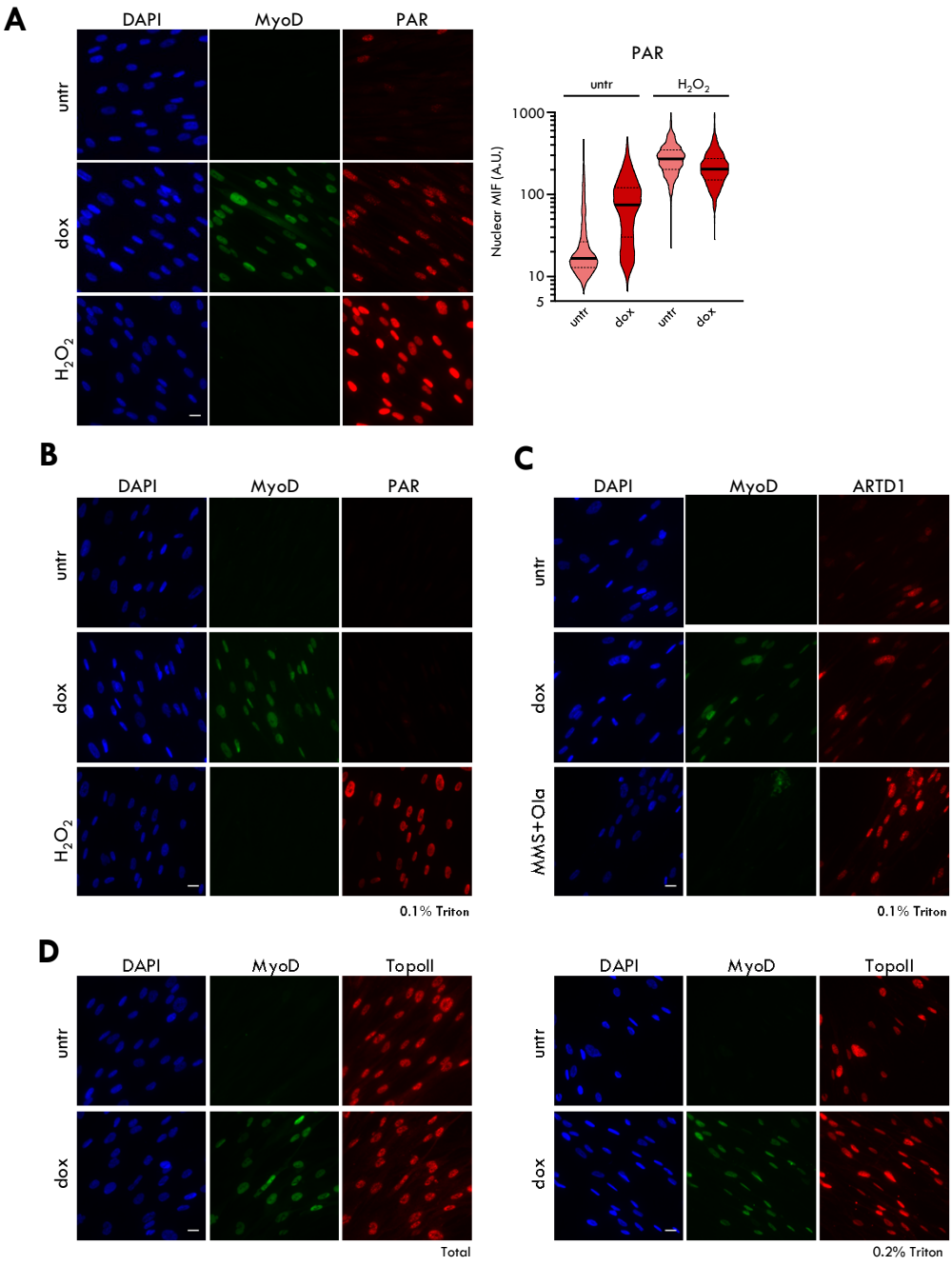
A
DAPI
MyoD
PAR
untr
dox
H2O2
PAR
untr
H2O2
1000
100
10
5
Nuclear MIF (A.U.)
untr
dox
untr
dox
B
DAPI
MyoD
PAR
untr
dox
H2O2
0.1% Triton
C
DAPI
MyoD
ARTD1
untr
dox
MMS+Ola
0.1% Triton
D
DAPI
MyoD
TopoII
untr
dox
Total
DAPI
MyoD
TopoII
untr
dox
0.2% Triton
E
WC
chr
soluble
untr
dox
MMS+ol
untr
dox
MMS+ol
untr
dox
MMS+ol
250-
130-
100-
ARTD1
55-
Tubulin
15-
H3

Suppl. Figure 6: MyoD-dependent ARTD1 is not associated to chromatin. Related to Figure 5.
(A) IF of untreated (untr) or dox-treated (dox) or H_2O_2-treated $MyoD^+$ fibroblasts using anti-MyoD and anti-PAR (magnification 20x). Scale bars indicate 20 μm. Quantification of PAR on the right. **(B)** IF for chromatin associated MyoD and PAR of $MyoD^+$ fibroblasts either untreated (untr) or dox-treated (dox) or treated with 1mM H_2O_2 after pre-extraction with 0.1% triton (magnification 20x). Scale bars indicate 20 μm. **(C)** IF for chromatin associated MyoD and ARTD1 of $MyoD^+$ fibroblasts either untreated or dox-treated or co-treated with Methyl methanesulfonate and olaparib (MMS + Ola) after pre-extraction with 0.1% triton (magnification 20x). Scale bars indicate 20 μm. **(D)** IF of $MyoD^+$ fibroblasts untreated or dox-treated using anti -Topoisomerase II (Topo II) antibody on total cells (left panel) or after pre-extraction with 0.2% Triton-X (right panel) (magnification 20x). Scale bars indicate 20 μm. (**E)** Chromatin fractionation followed by WB for ARTD1, tubulin and histone 3 (H3) of $MyoD^+$ fibroblasts untreated or dox-treated or co-treated with Methyl methanesulfonate and olaparib (MMS + Ola). (WC: whole cell; chr: chromatin fraction; soluble: soluble fraction).
For every quantification, the IF signal was normalised as described in Figure 1. The Y-axes of all violin plots are shown as log10 scales.

Suppl. Table 1: HiC depth, Related to Figure 2.

Sample ID	Sample name	Depth	Batch	Condition	Condition number
RLB1	Mock - Dox exp1	41.88982	1	-MyoD	1
RLB2	Mock + Dox exp1	44.82709	1	+MyoD	2
RLB3	A - Dox exp1	42.80994	1	siPARP -MyoD	3
RLB4	A + Dox exp1	50.45181	1	siPARP +MyoD	4
RLB5	Mock - Dox exp2	38.8991	2	-MyoD	1
RLB6	Mock + Dox exp2	44.89545	2	+MyoD	2
RLB7	A - Dox exp2	44.4141	2	siPARP -MyoD	3
RLB8	A + Dox exp2	33.72203	2	siPARP +MyoD	4
RLB9_B	A-A1 259	32.01774	3	siPARP -MyoD	3
RLB10_B	A-A1 NIR 259	30.55666	3	siPARP -MyoD +PARPi	5
RLB11_B	A-A1 DOX 259	31.23435	3	siPARP +MyoD	4
RLB12_B	A-A1 DOX NIR 259	30.43047	3	siPARP +MyoD +PARPi	6
RLB13_B	A-Mock 259	31.5787	3	-MyoD	1
RLB14_B	A-Mock NIR 259	31.21282	3	-MyoD +PARPi	7
RLB15_B	A-Mock DOX 259	29.76744	3	+MyoD	2
RLB16_B	A-Mock DOX NIR 259	31.69828	3	+MyoD +PARPi	8
RLB17_B	C-A1 NIR 259	30.13274	4	siPARP -MyoD +PARPi	5
RLB18_B	C-A1 DOX NIR 259	28.58152	4	siPARP +MyoD +PARPi	6
RLB19_B	C-Mock NIR 259	31.9398	4	-MyoD +PARPi	7
RLB20_B	C-Mock DOX NIR 259	30.82411	4	+MyoD +PARPi	8
RLB21	B- A1 259	26.18775	5	siPARP -MyoD	3
RLB22	B- A1 NIR 259	23.44518	5	siPARP -MyoD +PARPi	5
RLB23	B- A1 DOX 259	28.66356	5	siPARP +MyoD	4
RLB24	B- A1 DOX NIR 259	28.71846	5	siPARP +MyoD +PARPi	6
RLB25	B- Mock 259	25.07893	5	-MyoD	1
RLB26	B- Mock NIR 259	25.3203	5	-MyoD +PARPi	7
RLB27	B- Mock DOX 259	26.87696	5	+MyoD	2
RLB28	B- Mock DOX NIR 259	25.22572	5	+MyoD +PARPi	8

Suppl. Table 2: Summary table of Hi-C sample statistics, Related to Figure 2.

Condition	Sample	Sequenced Read Pairs	Uniquely mapped Read Pairs	% mapped	Valid Read Pairs	% Valid	% Cis/trans
siMock untr	1	44,187,561	36,954,764	83.6	31,578,703	85.5	76
	2	34,947,342	29,296,999	83.8	25,078,928	85.6	77
siMock dox	1	42,000,584	35,119,014	83.6	29,767,438	84.8	76
	2	37,365,353	31,336,077	83.9	26,876,956	85.8	75
siARTD1 untr	1	45,246,397	37,972,631	83.9	32,017,736	84.3	77
	2	36,672,196	30,804,333	84.0	26,187,747	85.0	76
siARTD1 dox	1	44,320,688	37,253,410	84.1	31,234,346	83.8	76
	2	39,898,741	33,473,561	83.9	28,663,557	85.6	75

A/B compartments analysis has been performed at 100 Kb resolution.

TRANSPARENT METHODS

Cell culture

The IMR90 cell line used for this study was originally purchased from Coriell Cell Repositories, grown under sterile conditions and routinely tested for mycoplasma. IMR90 cells were cultured in minimum essential medium (MEM) supplemented with 1% penicillin/ streptomycin (P/S), 10% (v/v) fetal calf serum (FCS), 1% non-essential Amino Acid solution (v/v) and 1% Sodium pyruvate (v/v, 1mM final concentration). After MyoD genetic complementation cells were cultured in presence of 1 µg/mL Puromycin to maintain the selection of cells with integrated constructs. HEK 293 cells were cultured in high glucose containing Dulbecco's modified Eagle's medium (DMEM) supplemented with 1% penicillin/ streptomycin (P/S) and 10% (v/v) FCS.

Genectic complementation of IMR90 cells with MyoD

MyoD integration was performed according to (Dall'Agnese et al., 2019) Briefly, using the Amaxa SE Cell Line 4D-Nucleofector Kit (Lonza), proliferating IMR90 cells at passage 7-9 were electroporated according to the manufacturer's protocol to introduce both the helper plasmid and the epB-Puro-TT containing murine MYOD cDNAand were then selected for the integration of the MyoD cDNA using 1 µg/mL of puromycin. Plasmids were kindly provided by P. L. Puri.

Trans-differentiation and terminal differentiation

The expression of MyoD in IMR90 cells was activated by addition of 50 ng/ml of doxycycline (dox). All experiments were performed in proliferating IMR90 cells at passage 18-25. For GM1 condition cells were seeded until 95% confluency, expression of MyoD was induced with 50 ng/ml dox and cells were collected 24h after dox addition. To induce the myogenic differentiation, expression of MyoD was induced with dox in 95% confluency IMR90 cells and after 24h the medium was exchanged with MEM supplemented with 1% penicillin/ streptomycin (P/S), 2% Horse serum (HS) and 1% Insulin-Transferrin-Selenium (ITS-G), 1% non-essential Amino Acid solution and 1% Sodium pyruvate (1mM final concentration), in presence of dox. Medium was exchanged every 2 days to add fresh dox. Cells were collected at day1 (DM1), day2 (DM2), day3 (DM3) or day5 (DM5) upon differentiation.
HEK 293 were transfected with helper plasmid and epB-Puro-TT containing murine MYOD cDNA in the same concentration as for IMR90. 2x BES solution (50nM N,N-bis(2-hydroxyethyl)-2-amino-ethanesulfonic acid (BES), pH 6.95 280 mM NaCl, 1.5mM Na_2HPO_4 in dd H_2O) was added dropwise to a mix of plasmid DNA and $CaCl_2$ yielding a final concentration of 1x BES and 150mM $CaCl_2$. After 2 min incubation at room temperature the mix was added to the cells drop-wise. Medium was changed after 6h. Cells were selected using 1.5 µg/mL of puromycin. Cells were seeded until 70% confluency, expression of MyoD was induced with 50 ng/ml of dox and cells were collected 24h (GM1), 48h (GM2) or 72h (GM3) after dox addition.

Drug treatments

Unless otherwise stated, cells were treated with the following compounds: H_2O_2 (1 mM, treatment performed in PBS) for 10 min, MMS (0.01% v/v) for 2h, Olaparib (10 µM) for 2h ,Niraparib (10 µM) for 24h and etoposide (5 µM) for 4 hrs.

siRNA transfection

siRNA mediated knock-down was performed via reverse transfection using Lipofectamine RNAi MAX according to the manufacturer's manual. In brief, the day after seeding cells in 3.5 cm dishes, 10 nM siRNA were mixed with 3 µl lipofectamine in 250 µl serum-free OptiMEM and incubated for 20 min at room temperature (RT) before being added dropwise unto the cells. 2 days after siRNA transfection, downstream experiments were performed. A scrambled siRNA was used as control for each experiment. If bigger dishes were used, volumes were up-scaled accordingly.

Immunofluorescence

For all IF experiments, cells were seeded on 12 mm glass coverslips, treated if required, and then fixed using 4 % FA for 15 min at RT. Cells were subsequently permeabilized for 10 min at RT in PBS with 0.2% Triton-X100 (Sigma Aldrich). When nuclear pre-extraction was performed, cells were first treated

with ice-cold permeabilization solution for 2 min on ice (unless stated otherwise) and then fixed as previously described. Cells were blocked in filtered PBS supplemented with 0.1% Triton-X100 and 2% BSA for 1h. The primary antibodies were diluted in blocking solution. By flipping the coverslips on drops of solution, cells were incubated with the antibody solution over night at 4°C. In case of the anti-PAR-Ab (Enzo), DMEM supplemented with 10% FCS was used for blocking and dilution of the primary antibody, which was incubated on the cells for 2h at RT. In case of the anti-MHC-Ab (DHSB), filtered PBS supplemented with 0.1% Triton-X100 and 3% BSA was used for blocking and dilution of the primary antibody, which was incubated on the cells for 1h at 37°C. All secondary antibodies were diluted in the standard blocking solution (0.1% Trition-X100 and 2% BSA in PBS) for 1h at RT. After each antibody incubation, cells were washed 3 times with PBS and then incubated with 0.1 µg/mL Dapi in PBS for 20 min at RT. After an additional PBS wash, the coverslips were briefly washed in distilled water and mounted on glass slides using 5.5 µl Mowiol solution per coverslip.

The following antibodies were used for IF at the indicated concentrations:, rabbit anti-PAR (Enzo, 1:1000), chicken anti-PAR (Abcam, 1:200), rabbit anti-PARP1 (46D11) (Cell Signalling, 1:500) mouse anti-MYOD (BD Bioscience, 1:250), mouse anti- myosin heavy chain (MHC) (DHSB, 1:10), mouse anti-H2A.X Phospho-ser 139 (Bio Legend, 1:1000), mouse anti-53BP1 (Upstate, 1:1000), mouse anti-H3K4me3 (Abcam, 1:1000), anti H3K9me2 (abcam, 1:500), rabbit anti-TopoII (abcam, 1:1000). Secondary antibodies: Alexa 488 goat anti-mouse (Thermo Fisher Scientific, 1:500), Cy3 goat anti-rabbit (Jackson Immunoreasearch, 1:250), Alexa488 goat anti-chicken (Jackson Immunoreasearch, 1:250).

Quantitative image-based cytometry (QIBC)

Automated multichannel wild-field microscopy for quantitative image-based cytometry was performed with the Olympus ScanR as previously described (Michelena et al., 2018). For each sample, at least1500 cells (were acquired using the UPLSAPO 20x objective (NA 0.9). For pre-extraction experiments a minimum of 100 cells was acquired. Every image was taken under non-saturating conditions and the same settings were used for all coverslips within the same experiment. The images were then analysed using the Olympus ScanR Image Analysis Software version 3.0.1, quantifying the mean fluorescence intensities within the nuclear masks. Using GraphPad Prism 8.0, the quantification of the mean fluorescence intensity was plotted as arbitrary units in violin plots and the signals for every event was normalized over the mean of the control/untreated, which was arbitrary set to 30. Each experiment was performed between 3 and 5 times and a representative graph from one experiment is shown. The Y-axes of all violin blots are depicted as log10 scales. For each experiment, representative pictures were chosen, where each channel was adjusted for brightness and contrast to the same settings. For statistical analysis, the normalized mean fluorescence intensity of 3 to 5 independent experiments were compared using a ratio-paired student t-test with *, $p<0.05$; **, $p<0.005$; ***, $p < 0.0005$.

Confocal microscopy

Confocal images were acquired on an automated CLSM – Leica SP8 upright confocal laser scanning microscope, equipped with 4 solid state diode lasers (405, 488, 552 and 638 nm), using an HCX PL APO CS2 63x immersion oil objective. For all images, brightness and contrast were adjusted using FIJI. For all images within one experiment, the same acquisition and image processing settings were used.

RNA extraction and quantitative PCR (qPCR)

RNA extraction was performed with the NucleoSpin RNA II kit (Macherey-Nagel) according to the supplier's protocol. RNA was quantified with a NanoDrop and reverse-transcribed using the High-Capacity cDNA Reverse Transcription Kit (Applied Biosystems) according to the supplier's protocol. Relative transcription levels were determined by normalizing to RPS27. qPCR was performed with KAPA SYBR FAST qPCR Kit (KAPA Biosystems) on a Rotor-Gene Qsystem (QIAGEN). Samples were run in duplicates and results are depicted as relative fold changes. All primers sequences are provided. For statistical analysis, 3 to 5 independent experiments were compared using a ratio-paired student t-test with *, $p<0.05$; **, $p<0.005$; ***, $p < 0.0005$.

RNA sequencing and bioinformatic analysis

Library preparation

The quality of the isolated RNA was determined using a Fragment Analyzer (Agilent, Santa Clara, California, USA). Only those samples with a 260 nm/280 nm ratio between 1.8–2.1 and a 28S/18S ratio within 1.5–2 were further processed. The TruSeq Stranded mRNA (Illumina, Inc, California, USA) was used in the succeeding steps. Briefly, total RNA samples (100-1000 ng) were poly A enriched and then reverse-transcribed into double-stranded cDNA. The cDNA samples were fragmented, end-repaired and adenylated before ligation of TruSeq adapters containing unique dual indices (UDI) for multiplexing. Fragments containing TruSeq adapters on both ends were selectively enriched with PCR. The quality and quantity of the enriched libraries were validated using the Fragment Analyzer (Agilent, Santa Clara, California, USA). The product is a smear with an average fragment size of approximately 260 bp. The libraries were normalized to 10nM in Tris-Cl 10 mM, pH8.5 with 0.1% Tween 20.

Cluster Generation and Sequencing
The Novaseq 6000 (Illumina, Inc, California, USA) was used for cluster generation and sequencing according to standard protocol. Sequencing were paired end at 2 X150 bp or single end 100 bp

Analysis
FastQC (Andrews) algorithm was used to check the quality of our fastq files and to identify the adaptor contamination and low quality regions of the reads. Subsequently, cutadapt algorithm was used to remove contaminations and low quality ends of the reads. STAR algorithm (Dobin et al., 2013) was used to align the RNASeq reads to hg38 human genome assembly. The gene transfer format (GTF) file of hg38 assembly was also obtained from UCSC database. Genome index was created using genome Generate function of STAR. Subsequently STAR align algorithm was implemented using fastq files generated by the sequencing. HTSeq algorithm (Anders et al., 2015) was used to profile expression counts from the binary format files that were created by STAR i.e. BAM files having alignment information and the HTSeq outputs in general text form were directed into a sperate folder. Two different R packages were used for expression profiling analysis. DESeq2 (Love et al., 2014) was used to detect differential expression in our RNASeq data. The other package used was edgeR (Robinson et al., 2010), which uses trimmed mean of M-values, (TMM) to normalize expression data. EstimateDisp function of edgeR was used to control false discovery rate. To plot gene expression data along the respective chromosomes we used karyoploteR (Gel and Serra, 2017) package together with homemade R script wrapper. GO terms enrichment analyses and bar plots of enrichments were performed using R packages and homemade R scripts. BiomaRT (Durinck et al., 2005) package was used to import entrez IDs of differentially expressed genes in different libraries of our RNASeq experiments and used clusterProfiler (Yu et al., 2012) package for the enrichment analyses. We extensively used ggplot2 (Wickham, 2009) package to generate high-quality plots with more details, as it provides more functionality for plot generation. Homemade scripts in R, unix bash and python together with R packages were used to process expression profile outputs of DESeq2. The tables and various plots including heatmaps were generated with homemade scripts and sometimes using available R packages like ComplexHeatmap (Gu et al., 2016), cluster (https://cran.r-project.org/web/packages/RColorBrewer/index.html.), circlize (Gu et al., 2014) and RColorBrewer (https://svn.r-project.org/R-packages/trunk/cluster).

Chromatin Immunoprecipitation sequencing
The analysis was performed as previously described (Dall'Agnese et al., 2019).

Hi-C
Library preparation
Hi-C experiments were performed as previously described (Rao et al., 2014) with some modifications (Vidal et al., 2018). Briefly, after cross-link with 1% formaldehyde and quenching with glycine (125 mM final), cell pellets were incubated in 3C lysis Buffer (10 mM Tris-HCl pH=8, 10 mM NaCl, 0.2% NP40, 1X anti-protease cocktail) for 30 minutes on ice, then were centrifuged for 5 minutes at 3,000 rpm and resuspended in 190 uL of NEBuffer2 1X (New England Biolabs – NEB). 10 µL of 10% SDS were added and cells were incubated for 10 minutes at 65ºC. After addition of Triton X-100 and 15 minutes incubation at 37ºC, nuclei were centrifuged 5 minutes at 3,000 rpm and resuspended in 300 uL of NEBuffer2 1X and digestion was performed overnight using 400 U MboI restriction enzyme (NEB). After filling-in the generated ends with biotinylated-dATP (1.5 µL of 10 mM dCTP; 1.5 µL of 10 mM

dGTP; 1.5 µL of 10 mM dTTP; 37.5 µL of 0.4 mM Biotin-dATP; 50U of DNA Polymerase I Large (Klenow) fragment in 300 µL NEBuffer2 1X; 45 minutes at 37ºC), ligation was performed 4 hours at 16°C using 10,000 cohesive end units of T4 DNA ligase (NEB). After reversion of the cross-link, DNA was purified and sonicated to using a Bioruptor Pico (Diagenode; 8 cycles; 20s on and 60s off). Biotinylated DNA was pulled down and End-repair, A-tailing and Illumina adaptors ligation steps were performed on beads. Hi-C libraries were sequenced on a NextSeq500.

Data processing
Hi-C data were processed using an in-house pipeline based on TADbit (Serra et al., 2017). Reads were mapped according to a fragment-based strategy: each side of the sequenced read was mapped in full length to the reference genome Human Dec. 2013 (GRCh38/hg38). TADbit filtering module was used to remove non-informative contacts and to create contact matrices as previously described (Serra et al., 2017). PCR duplicates were removed, and the Hi-C filters applied corresponded to potential non-digested fragments (extra-dandling ends), non-ligated fragments (dandling-ends), self-circles and random breaks. Contact matrices were normalized for sequencing depth and genomic biases using OneD (Vidal et al., 2018). A and B chromatin compartment analysis was performed at 100KB resolution as previously described (Lieberman-Aiden et al., 2009, Serra et al., 2017). PCA were performed using the eigenvalues obtained for all autosomes in the different samples. A/B compartments analysis has been performed at 100 Kb resolution

Chromatin fractionation
Chromatin fractionation was performed as in (Dalcher et al., 2020). Briefly, after trypsinization, 2 Mio IMR90 cells were washed with PBS and resuspended in chromatin fractionation buffer (10 mM Hepes pH 7.6, 150 mM NaCl, 3 mM MgCl2, 0.5% Triton X-100, 1 mM DTT, with addition of fresh cOmplete™ Protease Inhibitor Cocktail (Roche)). Incubation of cells for 30 min at room temperature was followed by Chromatin precipitation via centrifugation. Both total and chromatin fractions were further treated with MNase (S7 Micrococcal nuclease, Roche). Samples were then incubated in 1× Laemmli buffer (10% glycerol, 10 mM Tris pH 6.8, 2% SDS, 0.1 mg/ml bromphenolblue, 2% β-mercaptoethanol) at 95°C for 5 min and further processed by Western Blot.

Western blot
For western blot analysis, proteins were separated via SDS-page on a 10% SDS-polyacrylamide gel at 120V. A wet-transfer into a PVDF membrane was performed at 30 V over-night and membranes were blocked with 5% milk in TBS-T for 1h at RT. Primary antibodies were diluted in 1 % milk in TBST and incubated at 4°C over-night. After 3 washes, the secondary antibody, diluted in TBST, was incubated for 1h at RT. After another 3 washes, specific proteins/bands were visualized with the Odyssey infrared imaging system (LI-COR).
The following primary and secondary antibodies were used for western blot analysis at the indicated concentrations: mouse anti-ARTD1 (Santa-Cruz, 1:2000), rabbit anti-H3 (Abcam, 1:5000), mouse anti-tubulin (Sigma 1:10000), IRDye 800CW goat anti-rabbit IgG (1:15,000, LI-COR, P/N 925-32211), and IRDye 680RD Goat anti-Mouse IgG (1:15,000, LI-COR, P/N 925-68070).

Template image for graphical abstract and schemes from www.BioRender.com

REAGENTS LIST

Reagent	Source	Identifier Cat. N.
Antibodies		
anti-MyoD antibody	BD-Bioscience	554130; RRID:AB_395255
anti-PAR antibody	Enzo	ALX-210-890A-0100
anti-PAR antibody	Abcam	ab14460; RRID:AB_301240
anti-H3 antibody	Abcam	ab1791; RRID:AB_302613
anti-tubulin antibody	Sigma	T6199; RRID:AB_477583
anti-ARTD1 antibody for WB	Santa-Cruz	sc-53643; RRID:AB_785086
anti-ARTD1 (46D11) antibody for IF	Cell signalling	9532s; RRID:AB_659884
anti-Myosin heavy chain, sarcomere (MHC) antibody	DSHB	MF20; RRID:AB_2147781
anti-H2A.X Phospho (ser 139)	BioLegend	613402; RRID:AB_315795
anti-53BP1	Upstate	MAB3802; RRID:AB_2206767
anti-H3K4me3	Abcam	ab6000; RRID:AB_2118290
anti-H3K9me2	Abcam	ab1220; RRID:AB_449854
anti-TopoII	Abcam	ab58442; RRID:AB_883147
Alexa488 goat anti-mouse	ThermoFisher	A11029; RRID:AB_2534088
Cy3 goat anti-rabbit	Jackson immunoresearch	111-165-144; RRID:AB_2338006
Alexa488 goat anti-chicken	Jackson immunoresearch	103-545-155; RRID:AB_2337390
IRDye 800CW goat anti-rabbit IgG	Li-COR	925-32211; RRID:AB_2651127
IRDye 680RD Goat anti-Mouse IgG	Li-COR	925-68070; RRID:AB_2651128
Chemicals		
Dulbecco's modified Eagle's medium (DMEM)	ThermoFisher	61965-026
Minimum essemtial medium (MEM)	ThermoFisher	1109508
Penicillin-streptomycin	ThermoFisher	15140-122
Fetal bovin serum	ThermoFisher	
Horse serum	ThermoFisher	26050070
ITS	ThermoFisher	51500056
Sodium pyruvate	ThermoFisher	11360070
Non-essential amino acids	ThermoFisher	11140035
OptiMEM	ThermoFisher	31985-047
Puromycin	Sigma Aldrich	R8875-5G
Doxycycline	ThermoFisher	D9891-1G
Rucaparib	Adooq	A14182

Olaparib	Selleckchem	S1060
Niraparib	Adooq	A11026
Methyl Methanesulfonate	Sigma Aldrich	129925-25G
Hydrogen peroxide solution	Sigma Aldrich	H1009-100ml
Dapi	BioLegend	422801
Bovine serum albumin	Sigma Aldrich	A9418
Formaldehyde	Sigma Aldrich	47608
Mowiol 4.88	Calbiochem	475904
Triton-X	Sigma Aldrich	T8787-100ml
cOmplete™ Protease Inhibitor Cocktail	Roche	11836170001
S7 Micrococcal nuclease	Roche	10107921001
Critical Commercial Assays		
Lipofectamine RNAiMAX	ThermoFisher	13778-150
MultiScribe Reverse Transcriptase	ThermoFisher	4311235
KAPA Biosystems Sybr Fast qPCR Kit	Roche	KK4600
Experimental Models: Cell Lines		
IMR90, human (female origin)	Corriell Institute	I90
HEK 293T, human	ATCC	CRL3216

PRIMERS SEQUENCE

Primer name	**Sequence**
hMyogenin fw	AGGTTGTGGGCATCTGTAGG
hMyogenin rv	CTCTCACAGCGCCTCCTG
hMCK fw	TGCACCTGTTCTACTTCGGA
hMCK rv	CACCCCAAGTTCGAGGAGAT
hMyoD fw	CGGAACTGCTACGAAGGC
hMyoD rv	TCCACGATGCTGGACAGG
hRPS27 fw	GTGAAATGCCCAGGATGCTATA
hRPS27 rv	TGTAGGCTGGCAGAGGACAGT
hARTD1 fw	TCTTTGATGTGGAAAGTATGAAGAA
hARTD1 rv	GGCATCTTCTGAAGGTCGAT

SiRNA LIST

siRNA name	**Source**	**Identifier N.**
siARTD1	Qiagen	SI02662996

SUPPLEMENTAL INORMATION REFERENCES

Anders, S., P. T. Pyl, and W. Huber. 2015. 'HTSeq--a Python framework to work with high-throughput sequencing data', *Bioinformatics*, 31: 166-9.

Dalcher, D., J. Y. Tan, C. Bersaglieri, R. Pena-Hernandez, E. Vollenweider, S. Zeyen, M. W. Schmid, V. Bianchi, S. Butz, M. Roganowicz, R. Kuzyakiv, T. Baubec, A. C. Marques, and R. Santoro. 2020. 'BAZ2A safeguards genome architecture of ground-state pluripotent stem cells', *Embo Journal*, 39

Dall'Agnese, A., L. Caputo, C. Nicoletti, J. di Iulio, A. Schmitt, S. Gatto, Y. Diao, Z. Ye, M. Forcato, R. Perera, S. Bicciato, A. Telenti, B. Ren, and P. L. Puri. 2019. 'Transcription Factor-Directed Re-wiring of Chromatin Architecture for Somatic Cell Nuclear Reprogramming toward trans-Differentiation', *Molecular Cell*, 76: 453-72 e8.

Dobin, A., C. A. Davis, F. Schlesinger, J. Drenkow, C. Zaleski, S. Jha, P. Batut, M. Chaisson, and T. R. Gingeras. 2013. 'STAR: ultrafast universal RNA-seq aligner', *Bioinformatics*, 29: 15-21.

Durinck, S., Y. Moreau, A. Kasprzyk, S. Davis, B. De Moor, A. Brazma, and W. Huber. 2005. 'BioMart and Bioconductor: a powerful link between biological databases and microarray data analysis', *Bioinformatics*, 21: 3439-40.

Gel, B., and E. Serra. 2017. 'karyoploteR: an R/Bioconductor package to plot customizable genomes displaying arbitrary data', *Bioinformatics*, 33: 3088-90.

Gu, Z., R. Eils, and M. Schlesner. 2016. 'Complex heatmaps reveal patterns and correlations in multidimensional genomic data', *Bioinformatics*, 32: 2847-9.

Gu, Z., L. Gu, R. Eils, M. Schlesner, and B. Brors. 2014. 'circlize Implements and enhances circular visualization in R', *Bioinformatics*, 30: 2811-2.

Lieberman-Aiden, E., N. L. van Berkum, L. Williams, M. Imakaev, T. Ragoczy, A. Telling, I. Amit, B. R. Lajoie, P. J. Sabo, M. O. Dorschner, R. Sandstrom, B. Bernstein, M. A. Bender, M. Groudine, A. Gnirke, J. Stamatoyannopoulos, L. A. Mirny, E. S. Lander, and J. Dekker. 2009. 'Comprehensive mapping of long-range interactions reveals folding principles of the human genome', *Science*, 326: 289-93.

Love, M. I., W. Huber, and S. Anders. 2014. 'Moderated estimation of fold change and dispersion for RNA-seq data with DESeq2', *Genome Biol*, 15: 550.

Michelena, J., A. Lezaja, F. Teloni, T. Schmid, R. Imhof, and M. Altmeyer. 2018. 'Analysis of PARP inhibitor toxicity by multidimensional fluorescence microscopy reveals mechanisms of sensitivity and resistance', *Nat Commun*, 9: 2678.

Rao, S. S., M. H. Huntley, N. C. Durand, E. K. Stamenova, I. D. Bochkov, J. T. Robinson, A. L. Sanborn, I. Machol, A. D. Omer, E. S. Lander, and E. L. Aiden. 2014. 'A 3D map of the human genome at kilobase resolution reveals principles of chromatin looping', *Cell*, 159: 1665-80.

Robinson, M. D., D. J. McCarthy, and G. K. Smyth. 2010. 'edgeR: a Bioconductor package for differential expression analysis of digital gene expression data', *Bioinformatics*, 26: 139-40.

Serra, F., D. Bau, M. Goodstadt, D. Castillo, G. J. Filion, and M. A. Marti-Renom. 2017. 'Automatic analysis and 3D-modelling of Hi-C data using TADbit reveals structural features of the fly chromatin colors', *PLoS Comput Biol*, 13: e1005665.

Vidal, E., F. le Dily, J. Quilez, R. Stadhouders, Y. Cuartero, T. Graf, M. A. Marti-Renom, M. Beato, and G. J. Filion. 2018. 'OneD: increasing reproducibility of Hi-C samples with abnormal karyotypes', *Nucleic Acids Res*, 46: e49.

Wickham, H. 2009. 'ggplot2 Elegant graphics for data analysis'.

Yu, G., L. G. Wang, Y. Han, and Q. Y. He. 2012. 'clusterProfiler: an R package for comparing biological themes among gene clusters', *OMICS*, 16: 284-7.